Chapter 5: Biological evaluation and computational studies of phytoconstituents as Antidiabetic potential

5.1 Introduction

Diabetes mellitus is a predominant metabolic disease marked by persistently high blood sugar levels brought on by dysfunctional insulin secretion, action, or both (Hameed et al., 2015). In order to avoid problems including cardiovascular disease, neuropathy, and nephropathy, blood glucose levels must be effectively managed (Gross et al., 2005). Treatments for diabetes include insulin therapy, oral hypoglycemic medications including metformin, sulfonylureas, and DPP-4 inhibitors, as well as more recent therapies like SGLT2 inhibitors and GLP-1 receptor agonists. One therapeutic approach involves modulating enzymes involved in glucose metabolism, particularly α-A and α-G (Kumari et al., 2023a). These enzymes are essential for the breakdown of carbohydrates; α-A hydrolyzes large starch molecules into smaller disaccharides and oligosaccharides, while α-G further breaks these down into absorbable glucose molecules (Kumari et al., 2023b). By effectively reducing the digestion of carbohydrates, these enzymes can help suppress postprandial blood glucose rises. Besides enzyme inhibition, enhancing glucose uptake in peripheral tissues is critical for comprehensive diabetes management.

Phytochemicals have emerged as promising candidates for diabetes treatment due to their natural origin and potential for fewer side effects compared to synthetic drugs. They offer a viable alternative to conventional medications like acarbose, miglitol, and voglibose, which, despite their efficacy, are associated with adverse gastrointestinal effects (Kashtoh and Baek, 2022). Nevertheless, more investigation is required to completely comprehend their modes of action and maximize their therapeutic application.

Hemidesmus indicus is a medicinal plant known for its many therapeutic benefits, including anticancer, hypoglycemic, hypolipidemic, hepatoprotection, cardioprotection,

immunomodulation, antipyresis, anti-asthmatic, anti-arthritic, and antibacterial action (Baheti et al., 2006; Das and Singh Bisht, 2013; Ferruzzi et al., 2013; Mehta et al., 2012; Saritha et al., 2015). Its root contains bioactive compounds, including 2-hydroxy 4-methoxy benzoic acid, which has shown antidiabetic effects by suppressing gluconeogenesis and reducing blood glucose levels (Gayathri and Kannabiran, 2008). The root extract has also been found to lower fasting and postprandial glucose levels, as well as reduce low-density lipoprotein (LDL) and total cholesterol in diabetic models (Sowmia and Kokilavani, 2007). Additionally, it has been observed to impede the invitro diffusion of glucose across biomembranes, suggesting its potential to reduce intestinal glucose absorption (Archit et al., 2013). Furthermore, compounds such as Hemidesminine, β-sitosterol, Hemidesmin-1, and Hemidesmin-2 have shown aldose reductase inhibitory properties, which could help prevent diabetic complications like cataracts (Haroon et al., 2021).

Ichnocarpus frutescens also has various pharmacological activities, such as antidiabetic, antimicrobial, antioxidant, antihyperlipidemic, anti-inflammatory, anticancer, antipyretic, anti-asthmatic, anti-arthritic, antihyperlipidemic, hepatoprotective, and cardioprotective activities (D K Dash et al., 2007; Kharat and , Shylaja.H , G.L.Viswanatha, 2010b; Malathy N S, 2009; Pandurangan et al., 2009). Many phytoconstituents with antidiabetic potential are found in *Ichnocarpus frutescens*, including Sinapic acid, protocatechuic acid, lupeol, friedelin, β-sitosterol, ursolic acid, kaempferol, quercetin, and α-amyrin (Aggarwal et al., 2010). According to invivo research, *Ichnocarpus frutescens* root extract significantly lowers blood sugar levels in diabetic rats and Invitro investigations have shown that its polyphenolic extract can inhibit α-A and α-G enzymes, supporting its role in managing postprandial hyperglycemia (Kumarappan and Mandal, 2008; Kumarappan et al., 2007; Kumari et al., 2023c; Srujana et al., 2018). Notwithstanding these results, the

exact mechanisms through which *Hemidesmus indicus* and *Ichnocarpus frutescens* exert their antidiabetic effects remain to be fully understood. Various investigations have explored the antidiabetic potential of these plants, but there is limited information on the specific bioactive compounds responsible for α-A and α-G inhibition and their modes of action.

To address these gaps, this chapter aims to evaluate the antidiabetic potential of root extracts of *Hemidesmus indicus* and *Ichnocarpus frutescens* and isolated phytochemicals, specifically silychristin from *Hemidesmus indicus* and hyperoside from *Ichnocarpus frutescens*, on α-A and α-G enzymes. Additionally, studies for glucose uptake have been carried out using the 3T3-L1 cell line, which is generated from mouse fibroblasts. This model is frequently used to investigate the development and metabolism of adipocytes. These pre-adipocyte cells have the ability to differentiate into mature adipocytes under specific conditions, making them ideal for research related to obesity, diabetes, and metabolic disorders (Guru et al., 2021). The 2-NBDG glucose uptake assay will be utilized to provide a quantitative measure of glucose uptake in the presence of these phytochemicals (Bala et al., 2021). An increase in glucose uptake would suggest enhanced insulin sensitivity, which is crucial for effective diabetes management (Goldstein, 2002).

Considering that diabetes often impairs wound healing, leading to chronic wounds and ulcers, this chapter has also examined the impact of these bioactive compounds on wound healing processes (Blakytny and Jude, 2006). The 3T3-L1 cell line has been used in wound healing tests to evaluate the drugs' capacity to stimulate cell migration and proliferation, which are critical for tissue repair and wound closure. Enhancing wound healing could offer significant therapeutic benefits for diabetic patients (Oliveira et al., 2022). In addition to biological evaluations, computational methods have also been

employed to predict the interactions of ligands with α-A and α-G enzymes. By integrating invitro assays with computational study, this chapter aimed to evaluate of the antidiabetic potential of silychristin and hyperoside.

5.2 Materials

5.2.1 Chemicals and Reagents

The porcine α-A enzyme (EC 3.2.1.1.) and acarbose were supplied by Sigma-Aldrich Co., St Louis, USA. Himedia Laboratories provided starch. Para-nitrophenyl alpha-D-glucoside (pNPG), para nitrophenol (PNP), and yeast α-G enzymes were purchased from Sisco research laboratories (SRL).

Cell culture media (DMEM medium) and supplements (foetal bovine serum, streptomycin, penicillin) were procured from MP Biomedicals, Germany. The MTT reagent and Dulbecco's Phosphate Buffered Saline (DPBS) have been acquired from MP Biomedicals in Germany. Recombinant human insulin was sourced from Merck, while IBMX and dexamethasone were supplied by HiMedia, India. The fluorescent glucose analog 2-NBDG (Cat. No. 13195) was obtained from Invitrogen, ThermoFisher Scientific, USA. Trypsin-EDTA solution from HiMedia, India. 500 µM IBMX, 10 µM dexamethasone, and 10 µg/mL insulin were added to DMEM medium, which served as the cell differentiation medium. 0.5% FBS and 10 µg/mL insulin were added to DMEM without glucose, which served as the glucose uptake medium.

5.2.2 Cell Line and Culture Conditions

The National Centre for Cell Science (NCCS) in Pune, India, provided the 3T3-L1 mouse fibroblast cell line. The cell line was cultivated in DMEM media that was enhanced with 100 units/mL of penicillin, 0.1 mg/mL of streptomycin, and 10% fetal bovine serum (FBS). To ensure ideal growth conditions, the culture flasks were kept at 37°C in a humidified environment with 5% CO2.

5.3 Methods

5.3.1 α-Amylase Inhibition Assay

α-A inhibition by different solvent extracts of root of *Hemidesmus indicus* and *Ichnocarpus frutescens* was carried out according to the modified procedure outlined by Poovitha and Parani (Poovitha and Parani, 2016). 500 µl of root extracts of both plants and 500 µl porcine pancreatic α-A (EC 3.2.1.1; 0.5 mg/ml) were preincubated at 25 °C. 500 µl starch was dissolved in every test tube and left for another 10 minutes. The α-A enzyme and 1% starch were prepared using a 20 mM sodium phosphate buffer with 6.7 mM NaCl at a pH of 6.9. Following the incubation period, 1 ml of dinitrosalicylic acid (DNS) was added and heated in a water bath for 10 minutes to cease the enzyme reaction. After cooling and dilution, absorbance was taken at 540 nm using spectrophotometry. The same method was carried out for acarbose (positive control) as well as the isolated phytoconstituents, hyperoside and silychristin, over a concentration range of 150 to 900 µM. Acarbose is a clinically approved antidiabetic agent widely recognized for effectively inhibiting carbohydrate-hydrolyzing enzymes, making it a standard reference for such assays (Van de Laar, 2008).

In this, phosphate buffer was used as a solvent for the negative control. To compute the α-A inhibition potential, the following formula was used: -

$$\text{Inhibition percentage} = \left[\left(Abs_{control} - Abs_{sample}\right) \div Abs_{control}\right] \times 100$$

5.3.2. α-Amylase Mode of inhibition (MOI) Assay

The enzyme kinetics study was conducted employing the protocol given by Ahmed et al. (Ahmed et al., 2020). The root extract of both plants with the lowest IC_{50} value was selected for the MOI assay for α-A. Hyperoside and silychristin, as well as the standard reference compound, acarbose, concentrations of 300 µM, 600 µM, and 900 µM were chosen to conduct the assay. 250 µl of α-A and 250 µl of phytoconstituents were combined

in the first set of tubes. The second set of tubes contained 250 µl of phosphate buffer and 250 µl of α-A. Both sets of test tubes were preincubated for 10 minutes at 25 °C. 250 µl of starch with varying concentrations (0.5–5 mg/ml) was put into each set of tubes and again incubated. The mixtures were boiled for 10 minutes after adding 500 µl of DNS to stop the process. The absorbance was measured at 540 nm utilizing spectrophotometry. A maltose standard curve was used to calculate the reaction velocities from the estimated amount of reducing sugar. The MOI of phytoconstituents was assessed using the Lineweaver-Burk plot or double reciprocal plot (Bhatnagar et al., 2022). Lineweaver-Burk plot was plotted against 1/V versus 1/S, as shown below.

$$1/V = (Km/Vmax) \times 1/S + 1/Vmax$$

[where S is the concentration of the substrate, Km is the Michaelis-Menten constant, V is the beginning reaction rate, and Vmax is the maximum reaction rate].

5.3.3 α-Glucosidase inhibitory assay

According to a modified approach outlined by Karakaya et al., the α-G inhibitory activity of different solvent extracts of the root of *Hemidesmus indicus* and *Ichnocarpus frutescens* was assessed using p-nitrophenyl glucopyranoside (pNPG) as substrate (Karakaya et al., 2018). 3.0 mM pNPG solution and 1.0 U/ml α-G solution were prepared in 20 mM phosphate buffer at pH 6.9. 100 µl α-G was preincubated with 50 µl of plant extracts at a temperature of 37 °C for 10 min. To commence the reaction, 50 µl of the substrate was added and further incubated. The enzyme process was stopped by adding 2 ml of 0.1 M Na2CO3 and heating it in the water bath for ten minutes. The yellow-colored product para nitrophenol (PNP) liberated from pNPG was assessed at 405 nm wavelength to determine the α-G activity. The same procedure was carried out for acarbose (positive control) as well as the isolated phytoconstituents, hyperoside and silychristin, over a concentration range of 150 to 900 µM. Acarbose is a clinically approved antidiabetic

agent widely recognized for effectively inhibiting carbohydrate-hydrolyzing enzymes, making it a standard reference for such assays (Van de Laar, 2008). A blank was made by swapping out the enzyme with phosphate buffer for each concentration of each sample. In this, phosphate buffer was used as a solvent for the negative control. To compute the α-G inhibition potential, the following formula was used: -

$$\text{Inhibition percentage} = \left[\left(Abs_{control} - Abs_{sample}\right) \div Abs_{control}\right] \times 100$$

5.3.4 Mode of Inhibition (MOI) Assay for α-Glucosidase

A modified version reported by Kazeem et al. was used to investigate the MOI of α-G by phytoconstituents (Kazeem et al., 2013). The root extract of both plants with the lowest IC_{50} value was selected for the MOI assay for α-G inhibition. For the pure compounds, hyperoside and silychristin, as well as the standard reference compound, acarbose, concentrations of 300 µM, 600 µM, and 900 µM were chosen to conduct the assay.

400 µl of α-G and 200 µl of phytoconstituents were incubated in the first set of tubes. 200 µl of phosphate buffer (pH 6.9) and 400 µl of α-G were incubated for 10 minutes in the second set of test tubes. After adding 200 µl of pNPG solution at different doses (0.5–2 mg/ml) to each set of tubes, the tubes were further incubated. The reaction was then stopped by adding 2 ml of Na2CO3 and boiling it in the water bath for 5 minutes. Spectrophotometry was then used to measure absorbance at 405 nm. The amount of reducing sugar was calculated, and the data was then transformed into reaction velocities using the PNP standard curve. The MOI of phytoconstituents on α-G was identified graphically by plotting Lineweaver-Burk (1/V versus 1/S) as given below: -

$$1/V = (Km/Vmax) \times 1/S + 1/Vmax$$

[The onset reaction rate is denoted by V, the maximal reaction rate by Vmax, the substrate concentration by S, and the Michaelis-Menten constant by Km].

5.3.5 Cell line study

5.3.5.1 Cell Culture and Differentiation

The pre-adipocyte 3T3-L1 cell line was cultivated in DMEM with 100 units/mL of penicillin, 0.1 mg/mL of streptomycin, and 10% fetal bovine serum (FBS) as supplemented and incubated for 24 hours. During this incubation period, the cells attached to the culture plates and began proliferating (Choi et al., 2016; Teixeira et al., 2022). Once the cells reached confluence, the process of inducing differentiation into adipocytes was initiated. The growth medium was replaced with a differentiation medium in order to promote differentiation, which contains DMEM with additions of 1 µM dexamethasone, 500 µM IBMX, 1 µg/mL insulin, and 10% FBS for 3 days (Jia et al., 2012). During this period, the compounds within the medium stimulated the pre-adipocytes to begin the adipogenic process, leading to early adipocyte development. Following this induction phase, the DMEM supplemented with 10% FBS and 1 µg/mL insulin was used in place of the differentiation media. The cells were then allowed to further differentiate and mature into adipocytes over the next 2-3 days. By the end of this process, the 3T3-L1 pre-adipocytes had fully developed into mature adipocytes, which were then used for subsequent experimental analysis (Vishwanath et al., 2013).

5.3.5.2 Cytotoxicity Study

For the cytotoxicity analysis, the isolated phytoconstituents, hyperoside and silychristin, were tested on the differentiated 3T3-L1 adipocytes across a concentration range of 6.25 to 200 µg/mL by using the methodology given by Yordanov et al. with minor changes (Yordanov et al., 2013). Each well of a 96-well microtiter plate was added with 200 µL of cell suspension, and incubated for 24 hours. Following this incubation, the media was cautiously aspirated, and 200 µL of the test compounds hyperoside and silychristin were

introduced to each well. The plate was further incubated for 24 hours. DMSO (less than 0.1%) was used as the solvent and was included as a negative control.

After removing the drug-containing solution, 200 µL of the MTT reagent-containing medium was introduced to each well, resulting in a final MTT concentration of 0.5 mg/mL and incubated to enable the development of formazan crystals. Following incubation, 100 µL of DMSO was applied to each well, and formazan crystals were dissolved by gently shaking the plate on a gyratory shaker. The absorbance was measured using a microplate reader at 540 nm and cell viability was computed using the following formula:

$$\text{Cell viability (\%)} = [(Abs_{Treated\ cells}) \div Abs_{control\ cells}] \times 100$$

5.3.5.3 Glucose Uptake Assay

The 2-NBDG glucose uptake assay was conducted to assess the effects of hyperoside and silychristin on glucose uptake in 3T3-L1 adipocytes. After differentiation, the mature adipocytes were serum-starved in glucose-free DMEM for 6-12 hours to deplete endogenous glucose (Manaharan et al., 2013). During this stage, the test compounds were prepared in glucose-free DMEM, with both hyperoside and silychristin dissolved in DMSO, ensuring that the final DMSO concentration remained below 0.1% to avoid solvent interference. The cells were then treated with Hyperoside (6.25 µg/mL) and Silychristin (12.5 µg/mL) for 24 hours. In addition to these treatments, insulin (100 nM) was used as a positive control to stimulate glucose uptake, and non-treated cells served as a negative control (Luan et al., 2018). The cells were then incubated with 100 µM 2-NBDG, a fluorescent glucose analog, in glucose-free DMEM for 30-60 minutes at 37°C in a CO_2 incubator. This allowed the fluorescent analog to be taken up by the cells. To get rid of any leftover 2-NBDG, the cells were properly rinsed with cold PBS (Hasan et al., 2017).

The relative fluorescence units (RFUs) have been estimated using a fluorescent plate reader with excitation and emission wavelengths set at 485 nm and 535 nm, respectively, in order to quantify the glucose uptake (Semaan et al., 2018). Fluorescence was detected in the FL1 channel (525 nm), typically used for FITC detection. Cells were analyzed immediately after incubation. The RFUs were normalized to non-treated control cells, glucose uptake was expressed as a percentage relative to the control or insulin-treated cells, and the effects of silychristin and hyperoside at their respective amounts on glucose absorption were ascertained (Kumar et al., 2012).

5.3.5.4 Wound Healing Assay

The *invitro* scratch wound healing assay was conducted on 3T3-L1 adipocytes to assess the effect of silychristin and hyperoside on cell migration. This assay aimed to evaluate the extent of wound closure at 24- and 48-hours post-treatment, offering insights into the wound-healing potential of these phytochemicals. To create a monolayer, cells were cultivated in 12-well plates. When the cells reached approximately 70-80% confluency, a scratch wound was created using a sterile 200 µL pipette tip, applying uniform pressure to ensure consistency across all wells. After the scratch, the wound area was cleaned by gently washing with PBS to get rid of any debris or detached cells. (X. Liu et al., 2018).

After wound creation, the cells were treated with 12.5 µg/mL silychristin and 6.25 µg/mL hyperoside, both dissolved in serum-free DMEM. Non-treated wells served as the control group and cells were incubated for 24 hours and 48 hours to monitor the migration and wound-healing process (Derici et al., 2021). Wound closure images were taken at 0 hours, 24 hours, and 48 hours using an inverted phase-contrast microscope. These images allowed for the observation of cell migration into the wounded area, which enabled the calculation of the wound healing rate. Using ImageJ software, the wound area at each time point was assessed in order to accurately measure the wound closure (Rieger et al.,

2018; Suarez-Arnedo et al., 2020), and the following formula was utilized for measuring the percentage of wound closure (Abeje et al., 2022):

$$\text{Percentage Wound Closure} = \frac{(\text{Initial Wound Area} - \text{Remaining Wound Area})}{\text{Initial Wound Area}} \times 100$$

5.3.6 Computational Study

5.3.6.1 Ligands Selection and Preparation

The phytochemicals hyperoside and silychristin isolated from *Ichnocarpus frutescens* and *Hemidesmus indicus* were selected to study their antidiabetic potential compared to acarbose as positive control through molecular docking study. The three-dimensional structures of ligands were acquired from the PubChem database in SDF format (Kim, 2021, 2016). Ligands were converted into PDB format employing Open Babel tools for the lowest energy conformer option (O'Boyle et al., 2011). Ligands were ascribed to the incorporation of polar hydrogen, Gasteiger charge computation, and control of the torsion tree by selecting the root prior to molecular docking. Raccoon software was utilized to store the data in pdbqt file format (Forli et al., 2016).

5.3.6.2 Receptor preparation

The structure of α-A and α-G protein (PDB ID: 2QV4 and 3CTT) (Alegbe et al., 2019; Bharadwaj et al., 2018; El Bakri et al., 2018; Gani et al., 2020; Ibitoye et al., 2018; Mor and Sindhu, 2020; Ogunwa et al., 2019; Rehman et al., 2019; Shaaban et al., 2018; Sharma et al., 2020; Singh et al., 2019; Swargiary and Daimari, 2020) in 3D form was obtained from Protein Data Bank (Burley et al., 2019). The protein was prepared using BIOVIA Discovery Studio Visualizer http://3dsbiovia.com/products/(Biovia, 2017) and Pymol (DeLano, 2002). The protein structure was saved in PDB format after removing ions, water molecules, cofactors, and ligands for future analysis. Polar hydrogen atoms

were added to the protein using AutoDock tools. The receptor was then assigned Kollman charges as α-A.: -8.376 and α-G: -6.248 and saved in pdbqt format.

5.3.6.3 Molecular docking

Molecular docking was conducted utilizing Auto Dock 4.2 (MGL Tools 1.5.6) http://autodock.scripps.edu/ (Forli et al., 2016; Morris et al., 2009). The receptor was kept rigid during the docking, and the ligand molecules were flexible. The Centre grid box values for α-A receptor were set to X = 12.631, Y = 47.341, Z = 26.244, and for α-G, X = 1.098, Y = -16.366, Z = 20.523. The number of grid points was set as 50 × 50 × 50 in X, Y, and Z dimensions with a default grid space of 0.375 Å for both proteins. The box was positioned in the center of the active site pocket, having all binding site residues and imparting space for rotational and translational movement to ligands. To validate the molecular docking study, the native ligand was redocked onto the active site of the target protein using a RMSD value of less than 2 Å. The Lamarckian genetic algorithm was utilized with specific parameters, including a population size of 150, a maximum number of generations of 27000, and a maximum energy evaluation of 2500000 for 50 separate GA runs. After the completion of docking, the ligands based on binding energy (BE) were selected, and docking complexes were visualized using Maestro (Schrödinger Release 2022–2, https://www.schrodinger.com/maestro). The phytochemicals showing better binding affinity with protein were evaluated as the best α-A and α-G inhibitors.

5.3.6.4 Molecular Dynamics Simulation

To understand the stabilities of docked structure and the interaction mechanism of ligands with the receptor, Molecular Dynamic Simulation was carried out in triplicate using GROMAC 2020 software (Abraham et al., 2015; Pronk et al., 2013). MD simulation was also performed for the reference drug acarbose. Molecular Dynamic Simulation was conducted with 4000 frames for 100 ns at time steps of 25 Pico seconds to analyse the

stability of the complex (Dalal et al., 2022; Renganathan et al., 2021). The AMBER99SB force field was obtained with GROMACS to obtain the topology of proteins. On the other hand, for ligands, the GAFF force field was attained with ACPYPE (Sousa Da Silva and Vranken, 2012). In order to neutralize the system, counter ions were introduced after the complex was solvated in a dodecahedron box using the TIP3P water model, leaving at least 10 Å between the box boundary and the protein edge. Steric clashes were removed, and the system's energy was minimized until the maximum force was below 1000 kJ/mol/nm. The temperature was maintained at 310 K, the pressure was kept at 1 atm, and NVT followed by NPT of 1ns each were incorporated (Dhankhar et al., 2020b, 2020a). Thereafter, all the ligand-receptor complexes were submitted to MD simulation for 100 ns. After simulation, MD simulation results were analyzed to assessed the stability of complex (Agarwal et al., 2022; Nakano et al., 2009).

5.3.6.5 MM-GBSA calculation

After finishing the molecular dynamic simulation, the trajectories were further evaluated to comprehend the MM-GBSA (Molecular Mechanics with Generalized Bonn Surface Area), binding free energy of all the α-A and α-G complexes through the following equations:

$\Delta G_{binding} = \Delta G_{total} - T\Delta S$

$\Delta G_{total} = \Delta G_{complex} - [\Delta G_{protein} + \Delta G_{ligand}]$

Where $\Delta G_{binding}$ - free energy of the complex including entropic term; $\Delta G_{protein}$ - Energy of protein; ΔG_{ligand} - Energy of ligand; $T\Delta S$ - Interaction Entropy (Owoloye et al., 2022; Shao et al., 2023; Zhong et al., 2020).

To achieve the aforementioned goal, the gmx_mmpbsa tool was used to compute MM-GBSA utilizing the most recent 10 ns of simulated trajectories (Du et al., 2011).

Additionally, a per-residue decomposition analysis was performed to assess the energy contribution of individual amino acids in inhibitor binding. It was accomplished by utilizing the gmx_mmpbsa tool, which disintegrates the BE of every complex (Valdés-Tresanco et al., 2021).

5.4 Results and Discussions

5.4.1 α-Amylase Inhibition Assay

Figures 5.1 and 5.2 represent the percentage inhibition of α-A by various solvent extracts from the roots of *Hemidesmus indicus*, and *Ichnocarpus frutescens*. Table 5.1 represents the IC_{50} values for the α-A inhibition of various extracts from *Hemidesmus indicus* and *Ichnocarpus frutescens*, as well as isolated phytochemicals (hyperoside and silychristin) and the positive control (acarbose).

Table 5.1: IC_{50} values for the α-A inhibition of various extracts from *Hemidesmus indicus* and *Ichnocarpus frutescens*, as well as isolated phytochemicals (hyperoside and silychristin) and the positive control (acarbose)

Compound/Extract	IC_{50} Value (mg/mL or µM)
Hemidesmus indicus	
Methanol extract	4.19 ± 0.04 mg/mL
Ethyl acetate extract	8.56 ± 0.08 mg/mL
Chloroform extract	12.73 ± 0.16 mg/mL
Water extract	6.25 ± 0.13 mg/mL
Ichnocarpus frutescens	
Methanol extract	7.34 ± 0.22 mg/mL
Ethyl acetate extract	20.46 ± 0.71 mg/mL
Chloroform extract	14.96 ± 0.42 mg/mL
Water extract	9.60 ± 0.01 mg/mL
Isolated Phytochemicals and Acarbose	
Hyperoside	321 µM
Silychristin	447 µM
Acarbose (positive control)	772 µM

For *Hemidesmus indicus*, the methanol extract showed the highest inhibition percentage at 92.57 ± 1.36%, followed by the water extract (74.91 ± 1.15%), ethyl acetate extract (62.26 ± 0.38%), and chloroform extract (47.24 ± 1.90%). At a lower concentration of 2

mg/mL, there was minimal variation in the inhibitory activity of the methanol, ethyl acetate, and water extracts, while the chloroform extract exhibited a noticeably lower inhibition. However, with increasing concentrations, all extracts demonstrated significant increases in inhibition percentages. The IC_{50} values of *Hemidesmus indicus* were determined as 4.19 ± 0.04 mg/mL for the methanol extract, 8.56 ± 0.08 mg/mL for the ethyl acetate extract, 12.73 ± 0.16 mg/mL for the chloroform extract, and 6.25 ± 0.13 mg/mL for the water extract.

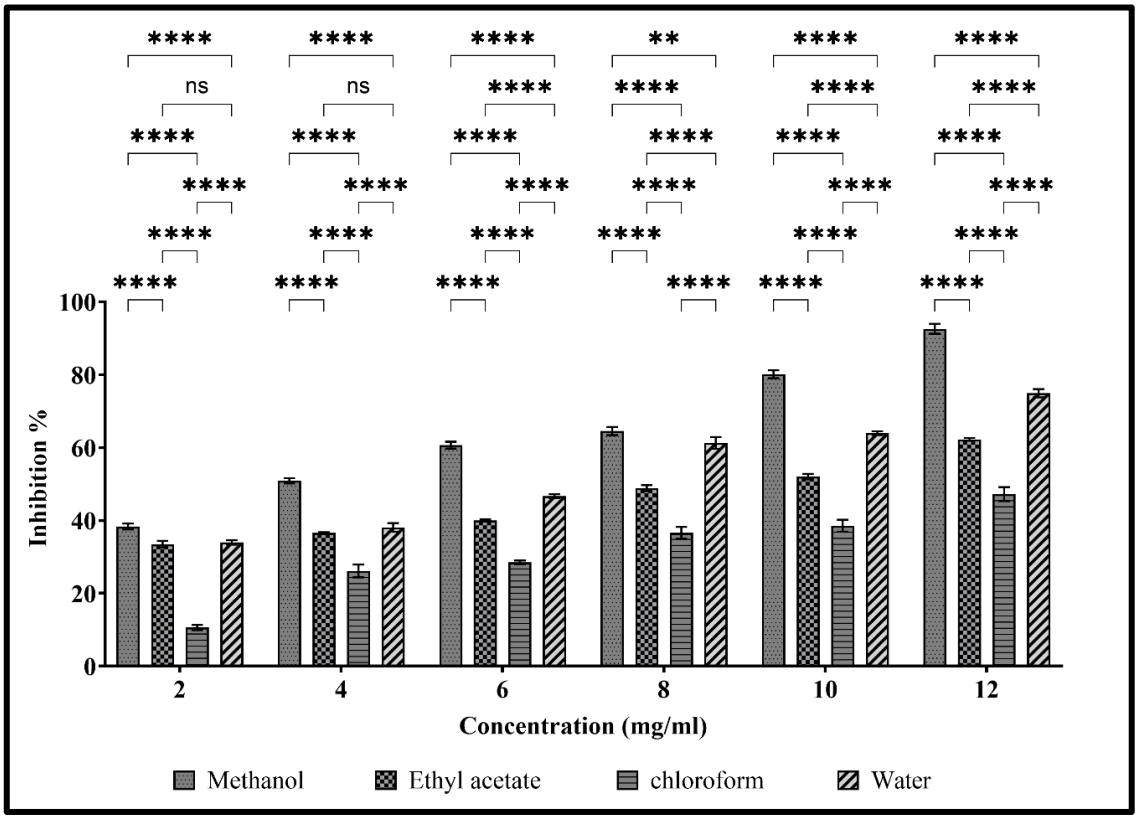

Figures 5.1: Percentage of α-A inhibition potential by the root of *Hemidesmus indicus*. Bars show mean ± SD; n = 3 independent replicates per concentration per solvent. Statistics were performed in GraphPad Prism using a two-way ANOVA (factors: solvent × concentration) followed by Tukey's multiple-comparisons post hoc test. Brackets denote the pairwise comparisons evaluated at each concentration. Significance: $P < 0.05$ (*), $P < 0.01$ (**), $P < 0.001$ (***), $P < 0.0001$ (****); ns = not significant ($P = NS$) (two-tailed, $\alpha = 0.05$).

For *Ichnocarpus frutescens*, the methanol extract exhibited the highest inhibition percentage at 72.25 ± 2.35%, followed by the water extract (60.26 ± 1.06%), chloroform extract (43.36 ± 1.21%), and ethyl acetate extract (27.34 ± 1.25%). Like *Hemidesmus*

indicus, the inhibition percentages of *Ichnocarpus frutescens* extracts increased significantly with rising concentrations. The IC_{50} value for the methanol extract was 7.34 ± 0.22 mg/mL, indicating the strongest α-A inhibition among the extracts. The IC_{50} values for the water, chloroform, and ethyl acetate extracts were 9.60 ± 0.01 mg/mL, 14.96 ± 0.42 mg/mL, and 20.46 ± 0.71 mg/mL, respectively. These results are consistent with previous studies on Adenanthera pavonina methanolic leaf extracts (Wickramaratne et al., 2016). The methanol extract showed the most potent α-A inhibition; therefore, it was selected for further enzyme inhibition kinetics studies.

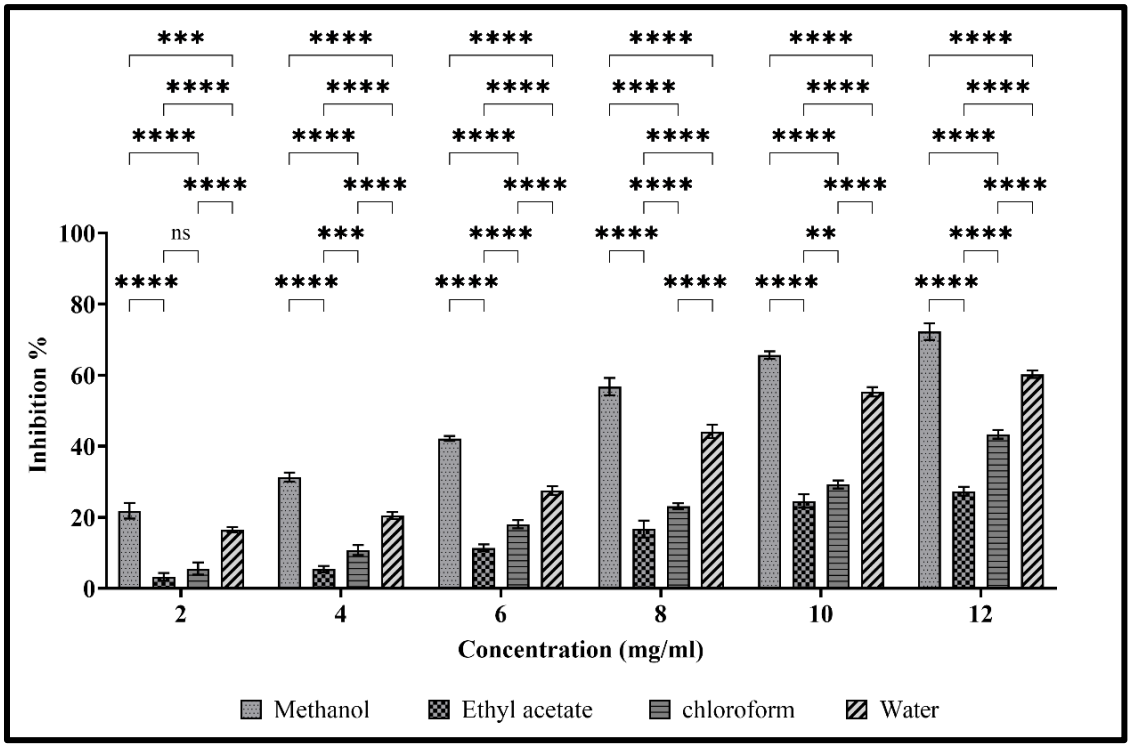

Figures 5.2: Percentage of α-A inhibition potential by the root of *Ichnocarpus frutescens*. Bars show mean ± SD; n = 3 independent replicates per concentration per solvent. Statistics were performed in GraphPad Prism using a two-way ANOVA (factors: solvent × concentration) followed by Tukey's multiple-comparisons post hoc test. Brackets denote the pairwise comparisons evaluated at each concentration. Significance: $P < 0.05$ (*), $P < 0.01$ (**), $P < 0.001$ (***), $P < 0.0001$ (****); ns = not significant ($P = NS$) (two-tailed, α = 0.05).

Figure 5.3 illustrates the α-A inhibitory potential of the isolated phytochemicals hyperoside and silychristin. The inhibition percentages for all three compounds were measured across a concentration range of 150 µM to 900 µM, offering insights into their

ability to inhibit α-A enzyme activity. At the highest concentration tested (900 μM), hyperoside showed the strongest inhibition, achieving an inhibition percentage of 78%, followed closely by silychristin with 69% inhibition. In contrast, acarbose exhibited a lower maximum inhibition of 61% at the same concentration. This pattern remained consistent across the concentration range, with hyperoside demonstrating the highest inhibitory potential, followed by silychristin, and then acarbose. In the intermediate concentration range (300–750 μM), hyperoside maintained its superior inhibitory activity over both silychristin and acarbose, with distinct differences in inhibition percentages. Silychristin also demonstrated stronger inhibitory properties compared to acarbose, further underscoring the potency of these natural compounds as α-A inhibitors. Hyperoside exhibited the lowest IC_{50} value of 321 μM, indicating its strong inhibitory capacity. The IC_{50} value of Silychristin was 447 μM, and acarbose had the highest IC_{50} value of 772 μM, making it the least effective inhibitor among the three.

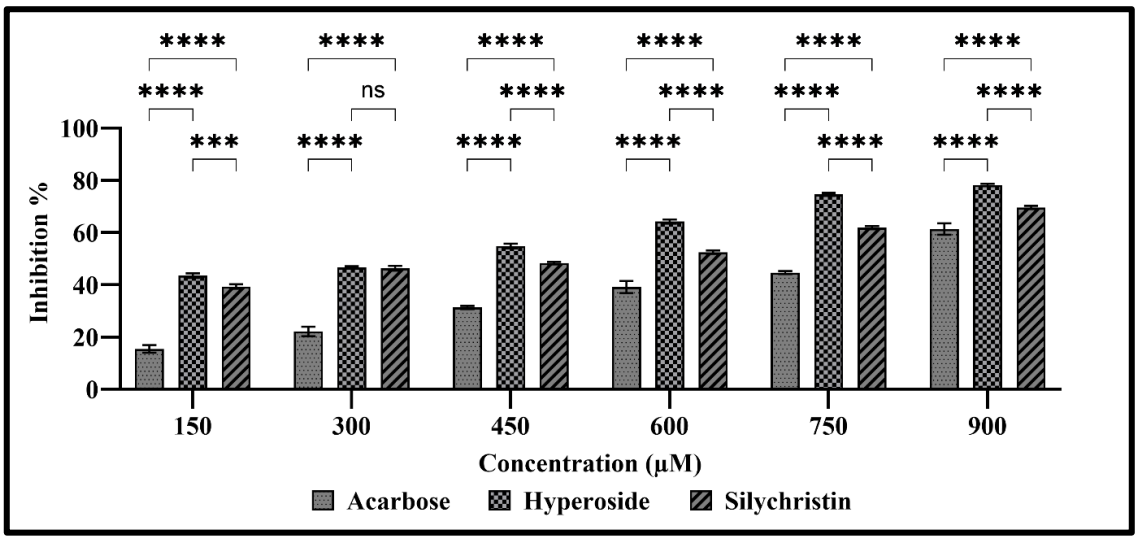

Figures 5.3: α-A inhibition percentage by the isolated phytochemicals hyperoside and silychristin, in comparison to the positive control, acarbose. Bars show mean ± SD; n = 3 independent replicates per concentration per compound. Statistics were performed in GraphPad Prism using a two-way ANOVA (factors: compound × concentration) followed by Tukey's multiple-comparisons post hoc test. Brackets indicate pairwise comparisons between compounds at each concentration. Significance: $P < 0.05$ (*), $P < 0.01$ (**), $P < 0.001$ (***), $P < 0.0001$ (****); ns = not significant ($P = NS$) (two-tailed, $\alpha = 0.05$).

5.4.2 Mode of α-Amylase Inhibition Assay

The MOI of α-A by the methanolic root extracts of *Hemidesmus indicus* and *Ichnocarpus frutescens* was evaluated using Lineweaver-Burk plots, as shown in Figures 5.4 and 5.5 respectively. The Km value for *Hemidesmus indicus* was higher when the inhibitor (extract) was present (0.519 mg/mL) than when it was absent (0.253 mg/mL), suggesting that α-A had a higher binding affinity for the inhibitor. In contrast, its affinity for the substrate (starch) decreased. The Vmax value remained constant at 4.7 mM/min, both with and without the inhibitor, indicating no change in the reaction rate.

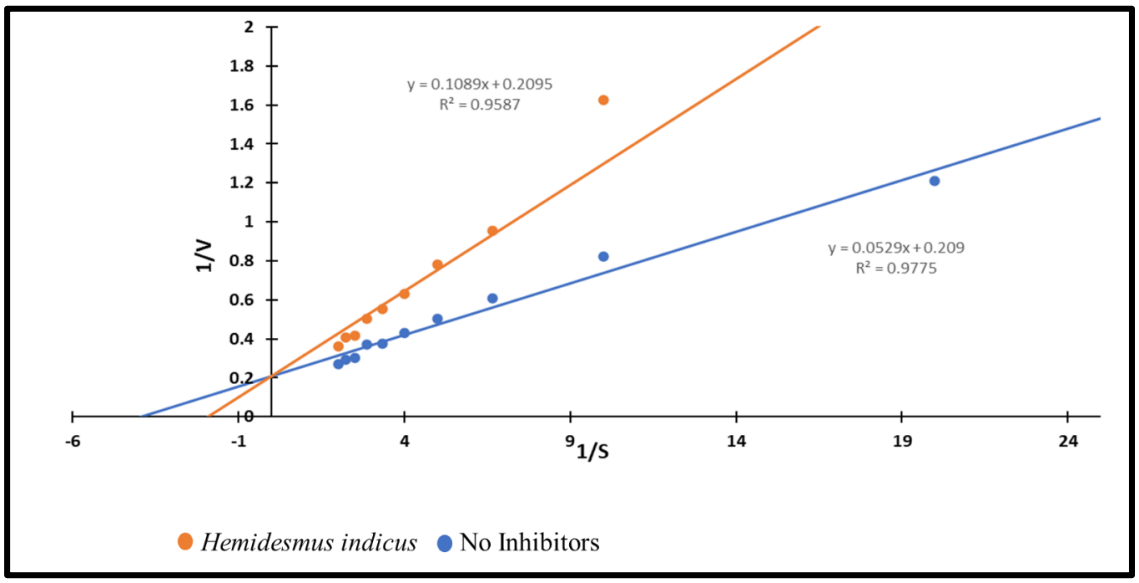

Figure 5.4: Mode of inhibition of α-A by methanolic root extract of *Hemidesmus indicus* using Lineweaver Burk plot.

For *Ichnocarpus frutescens*, the Lineweaver-Burk plot similarly demonstrated an increase in the Km value in the presence of the inhibitor (0.60 mg/mL) compared to the absence of the inhibitor (0.365 mg/mL), suggesting a higher binding affinity of α-A for the inhibitor and a reduced affinity for the substrate. The Vmax value remained unchanged at 8.116 mM/min, regardless of the presence or absence of the inhibitor. These kinetic parameters confirm that the methanolic root extracts of *Hemidesmus indicus* and *Ichnocarpus frutescens* act as competitive inhibitors of α-A. The competitive inhibition

suggests that the phytochemicals within these extracts compete with the substrate (starch) for binding, and effectively reduce enzyme activity (Matsuda et al., 2002).

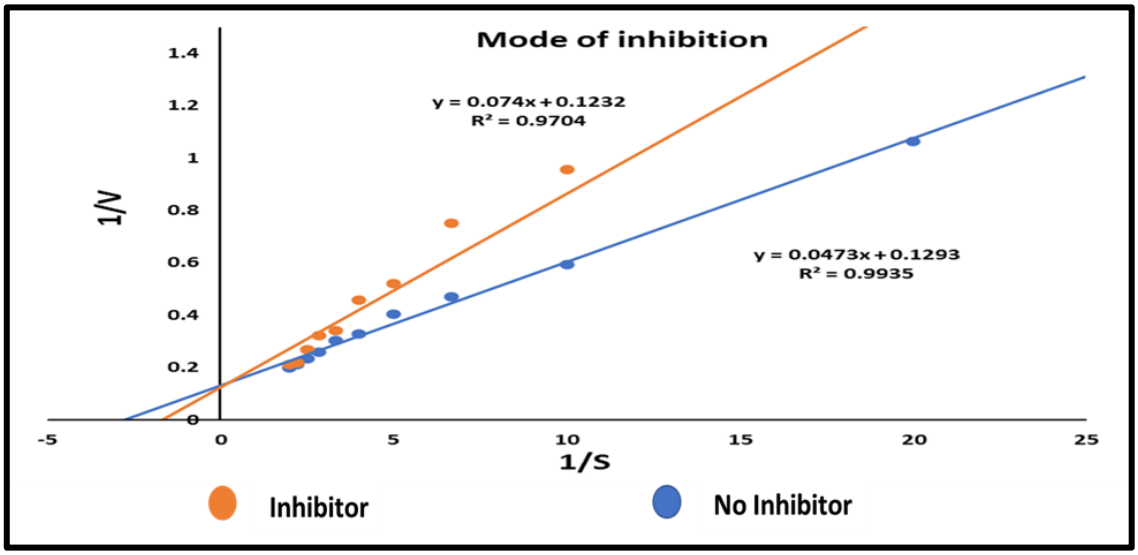

Figure 5.5: Mode of inhibition of α-A by methanolic root extract of *Ichnocarpus frutescens* using Lineweaver Burk plot.

The MOI of α-A by acarbose, hyperoside, and silychristin was assessed using Lineweaver-Burk plots to determine the inhibition type for each compound. The Lineweaver-Burk plots for acarbose, hyperoside, and silychristin at varying concentrations (0 µM, 300 µM, 600 µM, and 900 µM) are depicted in Figures 5.6, 5.7, and 5.8, respectively. For acarbose and hyperoside, the plots show a typical competitive inhibition pattern. As the concentration of the inhibitor increases (0 µM, 300 µM, 600 µM, 900 µM), the slope of the lines increases, but the lines intersect at the same point on the y-axis. This indicates that both acarbose and hyperoside compete with the substrate for binding at the enzyme's active site without altering the maximum velocity (Vmax). Among the two, hyperoside is the more effective inhibitor, with a Ki of -146.12 µM, compared to acarbose, which has a Ki of -364.58 µM, meaning hyperoside requires a lower concentration to inhibit 50% of the enzyme activity. In contrast, the Lineweaver-Burk plot for silychristin demonstrates a different inhibition pattern, characteristic of uncompetitive inhibition. The lines are parallel and do not intersect at the same point on

the y-axis, suggesting that silychristin binds only to the enzyme-substrate complex. This reduces both the Km and Vmax of the enzyme without affecting the binding affinity of the substrate. The Ki value for silychristin is -214.8 µM, indicating that it is a potent inhibitor, though with a different MOI compared to acarbose and hyperoside.

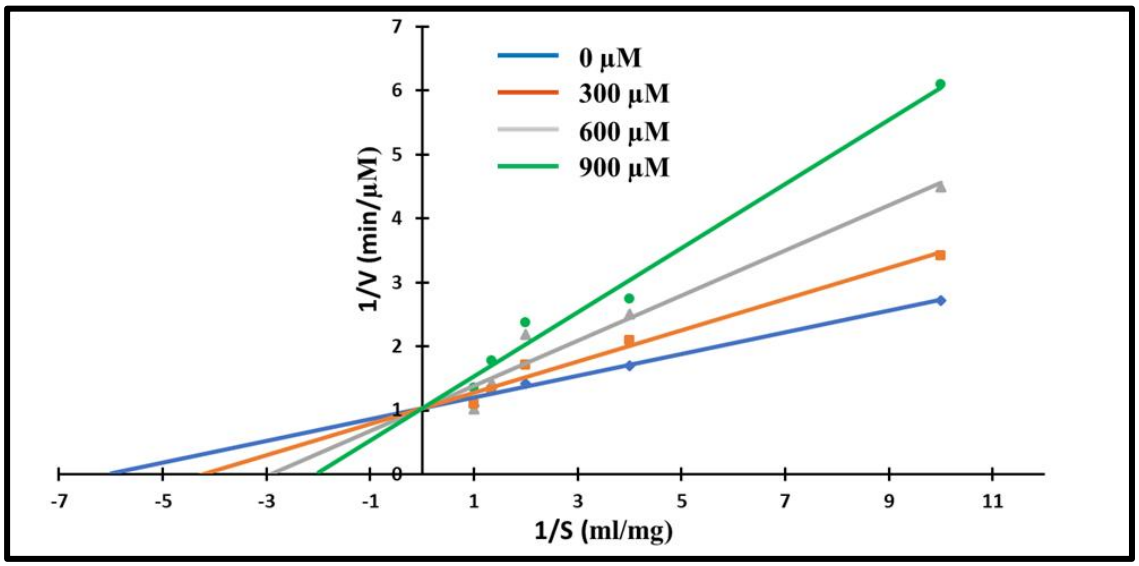

Figure 5.6: Mode of inhibition of α-A by acarbose using Lineweaver Burk plot.

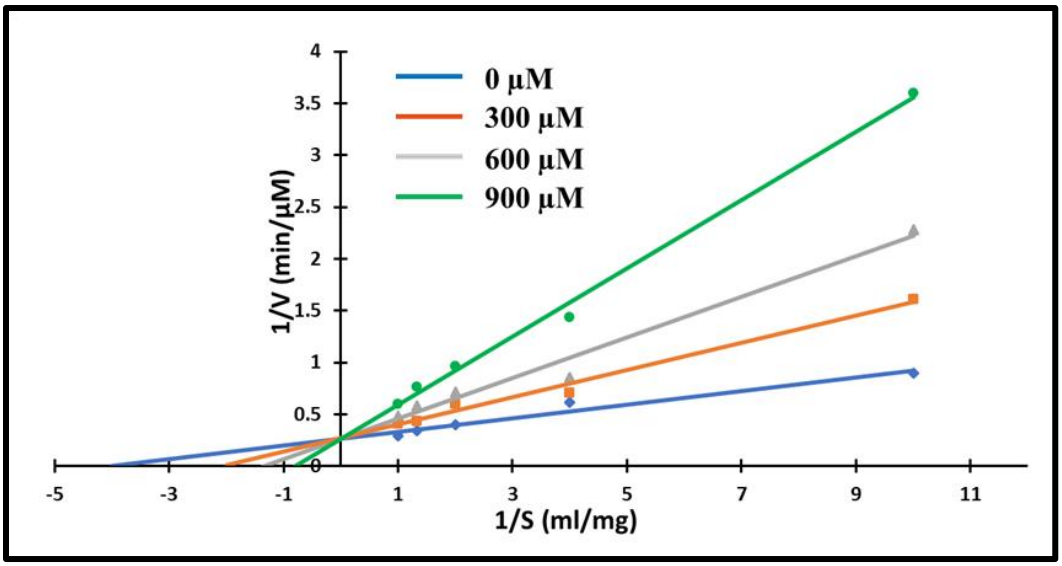

Figure 5.7: Mode of inhibition of α-A by hyperoside using Lineweaver Burk plot.

Thus, acarbose and hyperoside exhibit competitive inhibition, with hyperoside being the most potent of the two. On the other hand, silychristin shows uncompetitive inhibition, suggesting a unique mode of binding to the enzyme-substrate complex. Hyperoside is the

strongest inhibitor among the three, requiring the lowest concentration to inhibit 50% of α-A activity.

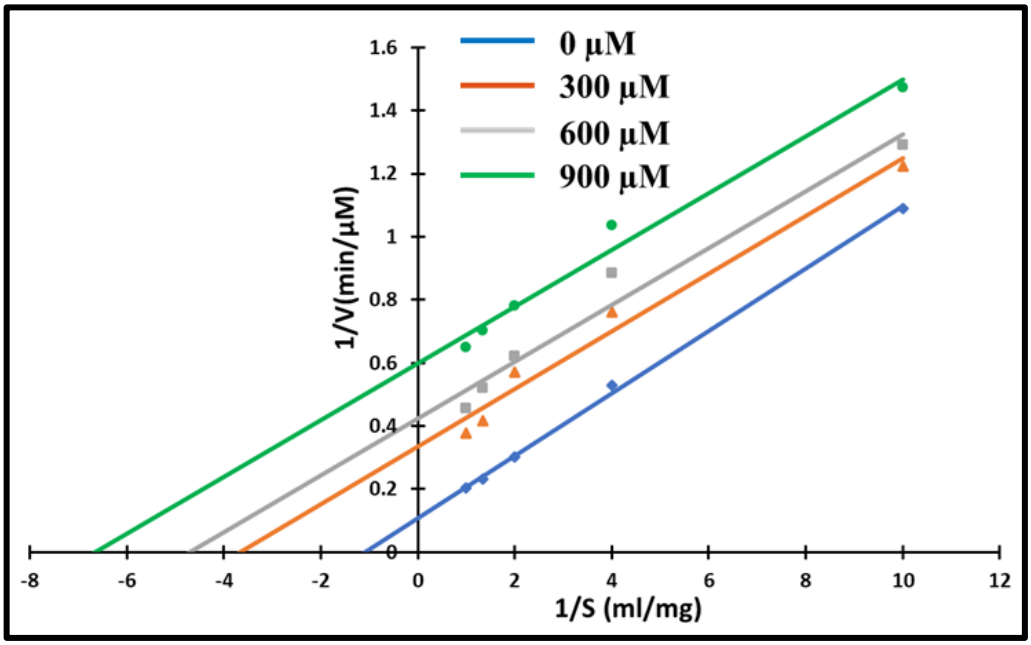

Figure 5.8: Mode of inhibition of α-A by silychristin using Lineweaver Burk plot.

5.4.3 α-Glucosidase Inhibition Assay

Figures 5.9 and 5.10 present the α-G inhibition profiles of solvent extracts of *Hemidesmus indicus* and *Ichnocarpus frutescens*, demonstrating a concentration-dependent increase in inhibitory activity across all solvent extracts. Table 5.2 represents the IC_{50} values for the α-A inhibition of various extracts from *Hemidesmus indicus* and *Ichnocarpus frutescens*, as well as isolated phytochemicals (hyperoside and silychristin) and the positive control (acarbose).

For *Hemidesmus indicus*, the methanol extract showed the highest α-G inhibition, reaching 73.05 ± 2.35%, followed by the ethyl acetate extract at 54.82 ± 0.95%. The water and chloroform extracts displayed similar inhibition percentages of 61.62 ± 1.12% and 60.53 ± 1.14%, respectively, at the highest concentration tested (12 mg/mL). Among the extracts, the methanol extract exhibited the strongest inhibitory potential with the lowest IC_{50} value of 5.78 ± 0.1 mg/mL. The IC_{50} values for the ethyl acetate, chloroform, and

water extracts were 11.54 ± 0.31 mg/mL, 9.32 ± 0.25 mg/mL, and 8.63 ± 0.21 mg/mL, respectively. For *Ichnocarpus frutescens*, the methanol extract displayed the highest inhibitory activity, achieving 86.27 ± 0.79% inhibition, followed by the chloroform extract at 69.22 ± 1.36%, the ethyl acetate extract at 65.59 ± 0.8%, and the water extract at 65.05 ± 1.39%. The methanolic extract also exhibited the strongest inhibitory potential with the lowest IC_{50} value of 4.40 ± 0.25 mg/mL. The IC_{50} values for the ethyl acetate, chloroform, and water extracts were 5.84 ± 0.03 mg/mL, 6.22 ± 0.33 mg/mL, and 8.61 ± 0.27 mg/mL, respectively.

Table 5.2: IC_{50} values for the α-G inhibition of various extracts from *Hemidesmus indicus* and *Ichnocarpus frutescens*, as well as isolated phytochemicals (hyperoside and silychristin) and the positive control (acarbose)

Compound/Extract	**IC_{50} Value (mg/mL or µM)**
Hemidesmus indicus	
Methanol extract	5.78 ± 0.1 mg/mL
Ethyl acetate extract	11.54 ± 0.31 mg/mL
Chloroform extract	9.32 ± 0.25 mg/mL
Water extract	8.63 ± 0.21 mg/mL
Ichnocarpus frutescens	
Methanol extract	4.40 ± 0.25 mg/mL
Ethyl acetate extract	5.84 ± 0.03 mg/mL
Chloroform extract	6.22 ± 0.33 mg/mL
Water extract	8.61 ± 0.27 mg/mL
Isolated Phytochemicals and Acarbose	
Hyperoside	191 µM
Silychristin	464 µM
Acarbose (positive control)	552 µM

These findings reveal that the methanolic extracts of both *Hemidesmus indicus* and *Ichnocarpus frutescens* demonstrated the lowest IC_{50} values, indicating that they possess the most potent α-A and α-G inhibitory activity. This outcome is due to unique physicochemical properties of methanol, which make it highly effective for extracting bioactive compounds from plants. Methanol possesses a low molecular weight, relatively high polarity, and strong hydrogen-bonding capacity, which enables it to efficiently

penetrate plant cell walls and membranes, disrupt intracellular hydrogen-bonding networks, and solubilize and extract a wide range of medium to high-polarity secondary metabolites, especially phenolic acids, flavonoids, and glycosides high-polarity secondary metabolites (Do et al., 2014b; Rice-Evans et al., 1997). As detailed in Chapter 3, Section 3.3.3, the methanolic extracts of both plants showed the highest total phenolic and flavonoid content among all tested solvents. These metabolites have potential for inhibition of α-amylase and α-glucosidase, antioxidant protection of pancreatic β-cells, modulation of insulin secretion, and improved glucose uptake (Kumar and Pandey, 2013).

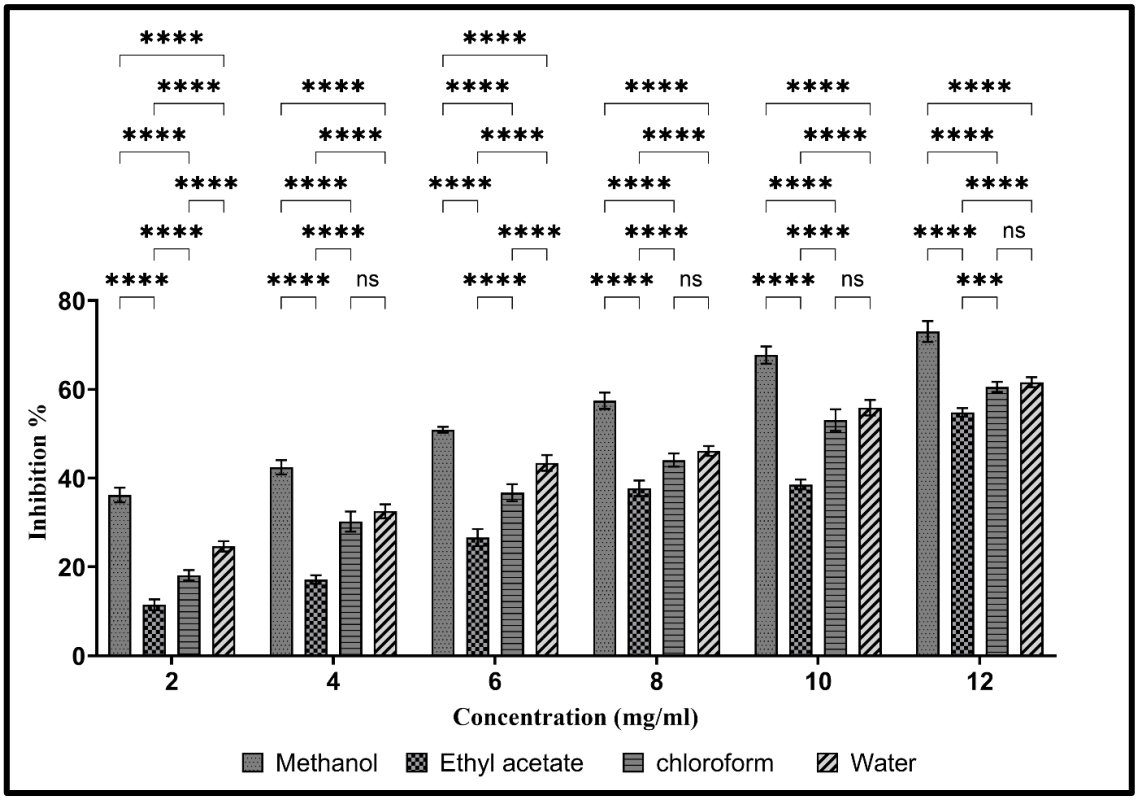

Figures 5.9: Percentage of α-G inhibition potential by the root of *Hemidesmus indicus*. Bars show mean ± SD; n = 3 independent replicates per concentration per solvent. Statistics were performed in GraphPad Prism using a two-way ANOVA (factors: solvent × concentration), followed by Tukey's multiple-comparisons post hoc test. Brackets indicate pairwise comparisons at each concentration. Significance: $P < 0.05$ (*), $P < 0.01$ (**), $P < 0.001$ (***), $P < 0.0001$ (****); ns = not significant ($P = NS$) (two-tailed, $\alpha = 0.05$).

Although water is more polar than methanol, it often co-extracts excess sugars, proteins, and other hydrophilic impurities that may dilute or interfere with bioactivity assays

(Kumar and Pandey, 2013). Several studies on plants such as *Hymenocardia acida* (Ezeigbo and Asuzu, 2012), *Ocimum tenuiflorum* (Mousavi et al., 2016), and *Amaranthus* spp. (Sangameswaran and Jayakar, 2008) reported that methanol extracts showed superior blood glucose-lowering activity relative to other solvent extracts. Analytical comparisons confirm that methanol extracts consistently yield higher total phenolic and flavonoid content, correlating with stronger in vitro and in vivo antidiabetic effects (Kumar and Pandey, 2013; Sultana et al., 2009). Therefore, the methanol extracts were selected for further studies on enzyme inhibition kinetics due to their superior inhibitory potential.

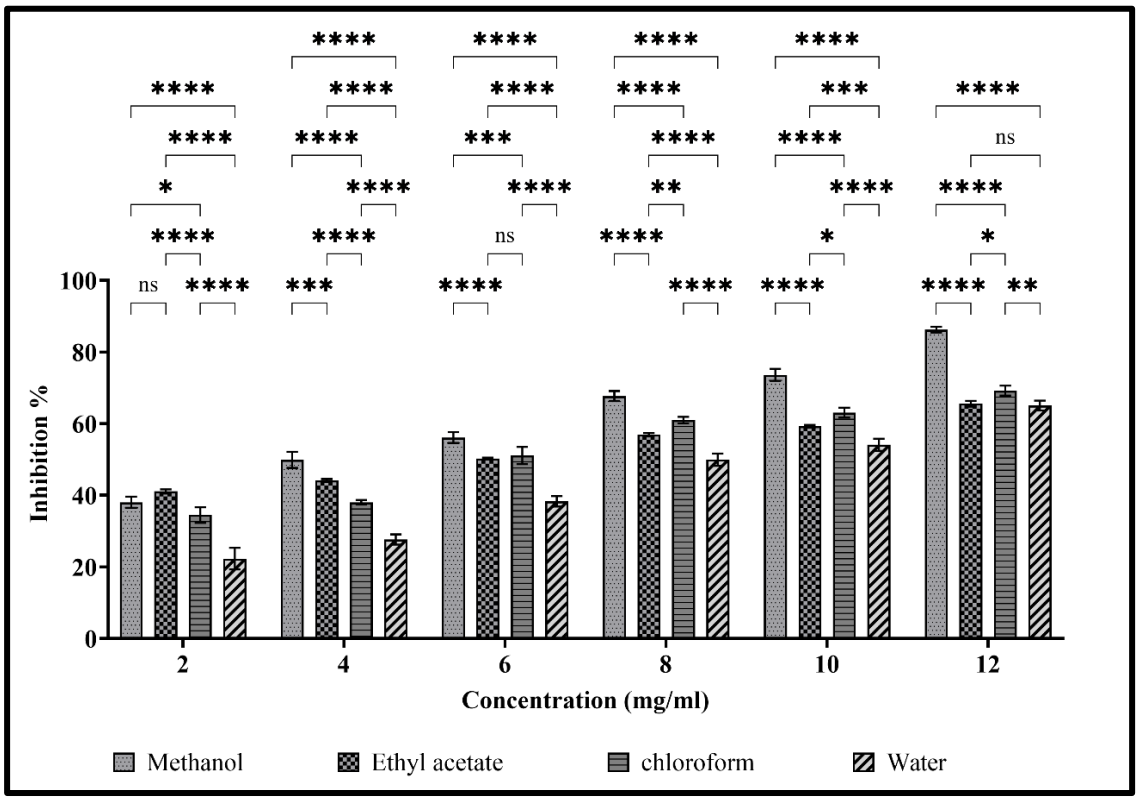

Figures 5.10: Percentage of α-G inhibition potential by the root of *Ichnocarpus frutescens*. Bars show mean ± SD; n = 3 independent replicates per concentration per solvent. Statistics were performed in GraphPad Prism using a two-way ANOVA (factors: solvent × concentration), followed by Tukey's multiple-comparisons post hoc test. Brackets indicate pairwise comparisons at each concentration. Significance: $P < 0.05$ (*), $P < 0.01$ (**), $P < 0.001$ (***), $P < 0.0001$ (****); ns = not significant ($P = NS$) (two-tailed, $\alpha = 0.05$).

Figure 5.11 illustrates the α-G inhibitory potential of the isolated phytochemicals hyperoside and silychristin, in comparison to the positive control, acarbose. The inhibition percentages for all three compounds were measured across a concentration range of 150 µM to 900 µM, offering insights into their ability to inhibit α-G enzyme activity. At the highest concentration tested (900 µM), hyperoside exhibited the strongest inhibition, achieving 83%, followed closely by silychristin at 82%. In contrast, the positive control, acarbose, showed a lower inhibition percentage of 59%. Across all concentrations, hyperoside consistently demonstrated the highest inhibitory potential, followed by silychristin, while acarbose consistently showed the lowest inhibition percentage at each concentration. At intermediate concentrations (450 µM to 750 µM), both hyperoside and silychristin maintained significantly higher inhibition levels compared to acarbose. The IC_{50} values further highlight the differences in potency between the compounds.

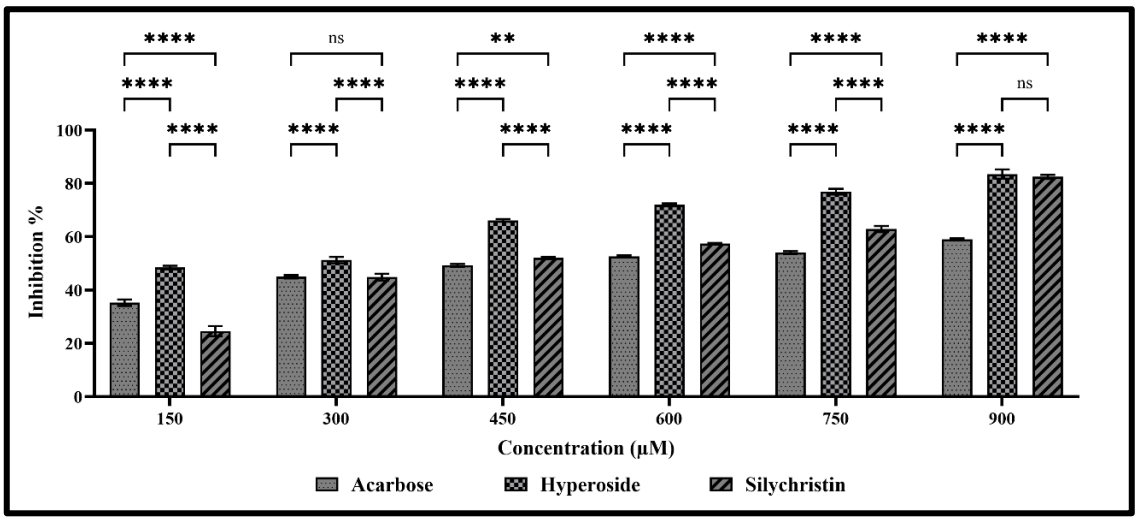

Figures 5.11: α-G inhibition percentage by the isolated phytochemicals hyperoside and silychristin, in comparison to the positive control, acarbose. Bars show mean ± SD; n = 3 independent replicates per concentration per compound. Statistics were performed in GraphPad Prism using a two-way ANOVA (factors: compound × concentration) followed by Tukey's multiple-comparisons post hoc test. Brackets indicate pairwise comparisons between compounds at each concentration. Significance: $P < 0.05$ (*), $P < 0.01$ (**), $P < 0.001$ (***), $P < 0.0001$ (****); ns = not significant ($P = NS$) (two-tailed, $\alpha = 0.05$).

Hyperoside exhibited the lowest IC_{50} value of 191 µM, indicating its superior inhibitory strength. Silychristin followed with an IC_{50} of 464 µM, showing greater inhibition than acarbose. Acarbose, with an IC_{50} value of 552 µM, was the least potent inhibitor among the three. Thus, the results demonstrate that both hyperoside and silychristin are more effective α-G inhibitors than the commonly used antidiabetic drug acarbose. Hyperoside, with its lowest IC_{50} value and consistently high inhibition percentages across all tested concentrations, proves to be the most potent inhibitor. Silychristin also shows strong inhibitory potential, though less effective than hyperoside.

5.4.4 Mode of α-Glucosidase Inhibition Assay

To investigate the kinetics of α-G enzyme inhibition, the methanol root extract of *Hemidesmus indicus* and *Ichnocarpus frutescens* was utilized due to its lowest IC_{50} value and the Lineweaver-Burk plot depicted in Figures 5.12 and 5.13. For *Hemidesmus indicus*, the presence of the inhibitor (extract) resulted in an increased Km value (0.586 mg/mL) compared to its absence (0.183 mg/mL), indicating that the binding affinity of α-G for the inhibitor was enhanced, while its affinity for the substrate (starch) decreased. The Vmax value remained constant at 9.67 mM/min, both with and without the inhibitor, indicating no change in the reaction rate.

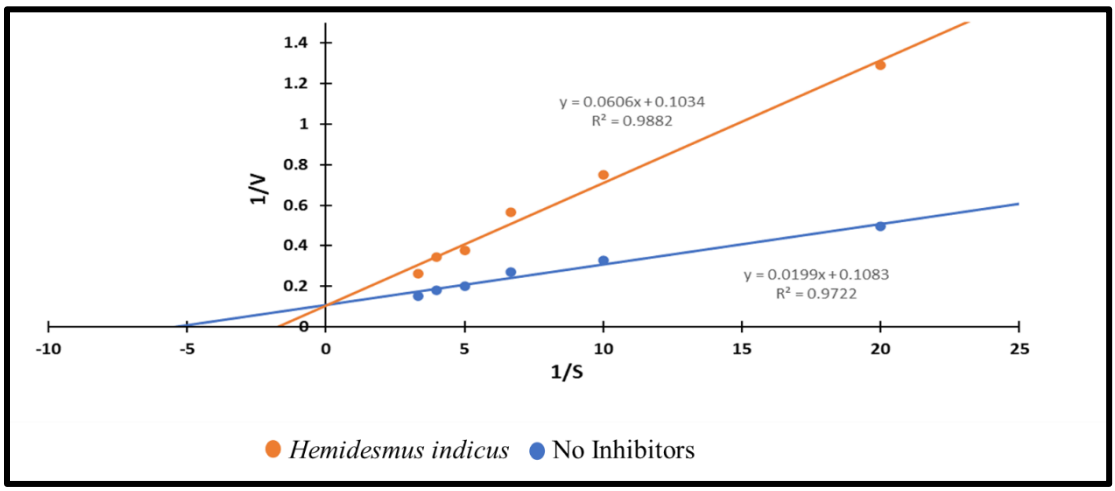

Figure 5.12: Mode of inhibition of α-G by methanolic root extract of *Hemidesmus indicus* using Lineweaver Burk plot.

For *Ichnocarpus frutescens*, the Lineweaver-Burk plot similarly demonstrated an increase in the Km value in the presence of the inhibitor (0.48 mg/mL) compared to the absence of the inhibitor (0.16 mg/mL), suggesting a higher binding affinity of α-G for the inhibitor and a reduced affinity for the substrate. The nearly identical Vmax values obtained with (24.6 mM/min) and without (23.2 mM/min) inhibitors indicate that the reaction rate remains unaffected. These kinetic parameters confirm that the methanolic root extracts of *Hemidesmus indicus* and *Ichnocarpus frutescens* act as competitive inhibitors of α-G. The competitive inhibition suggests that the phytochemicals within these extracts compete with the substrate (starch) for binding to the active site of the enzyme, effectively reducing enzyme activity (Matsuda et al., 2002).

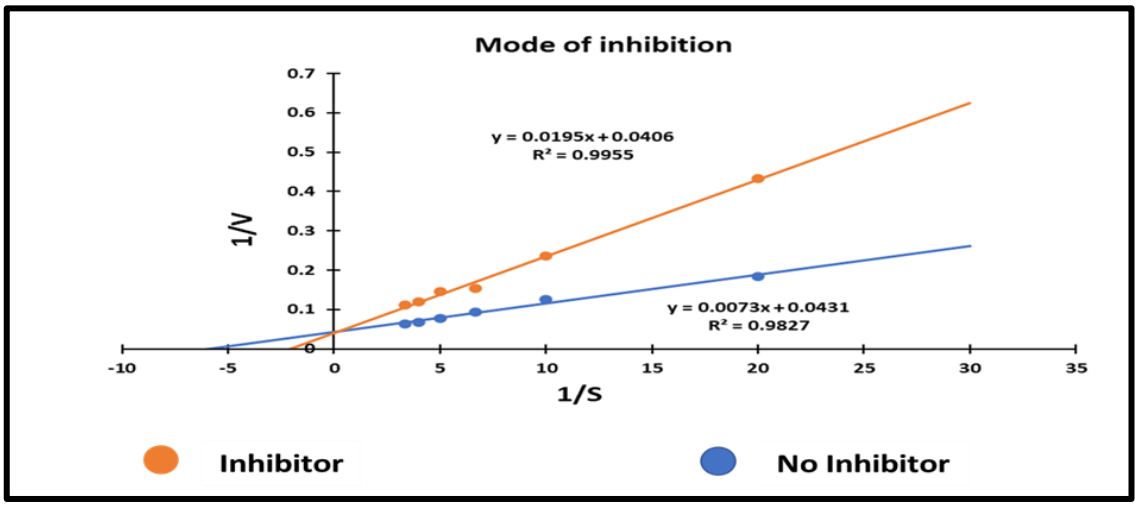

Figure 5.13: Mode of inhibition of α-G by methanolic root extract of *Ichnocarpus frutescens* using Lineweaver Burk plot.

The MOI of α-G by acarbose, hyperoside, and silychristin was also assessed using Lineweaver-Burk plots to provide insight into the inhibition type for each compound. Lineweaver-Burk plot for acarbose, hyperoside, and silychristin at varying concentrations (0 µM, 300 µM, 600 µM, and 900 µM) has been depicted in Figures 5.14, 5.15, and 5.16.

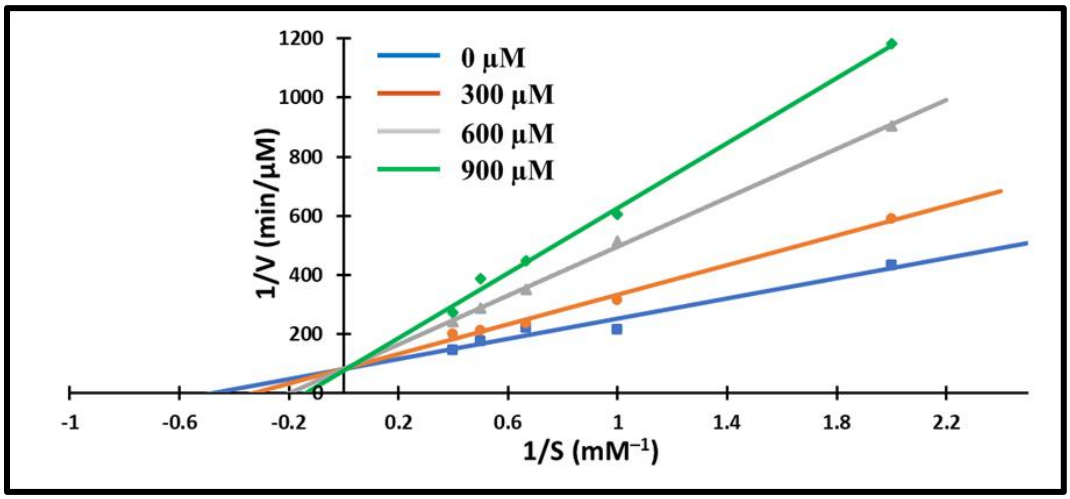

Figure 5.14: Mode of inhibition of α-G by acarbose using Lineweaver Burk plot.

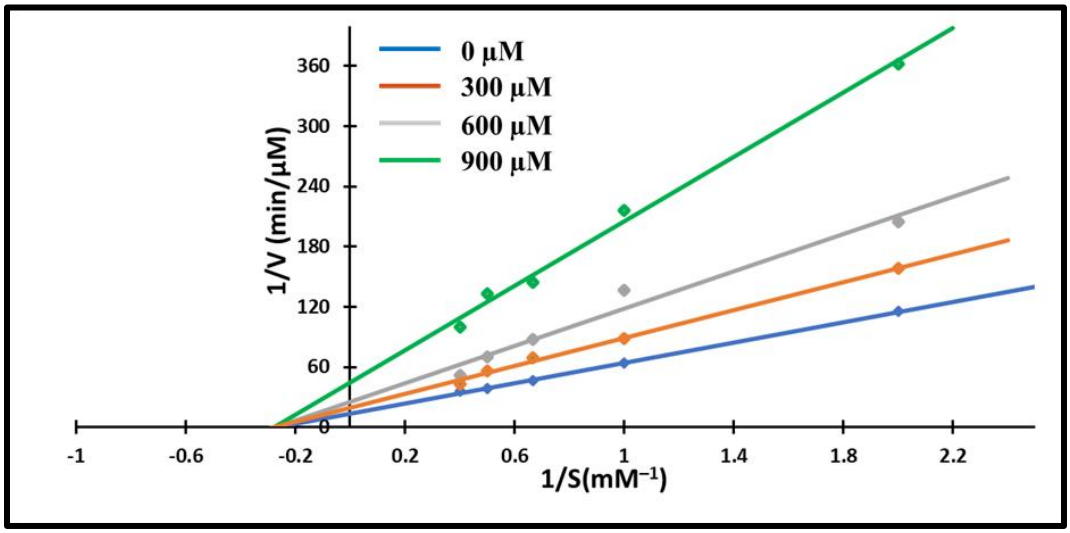

Figure 5.15: Mode of inhibition of α-G by hyperoside using Lineweaver Burk plot.

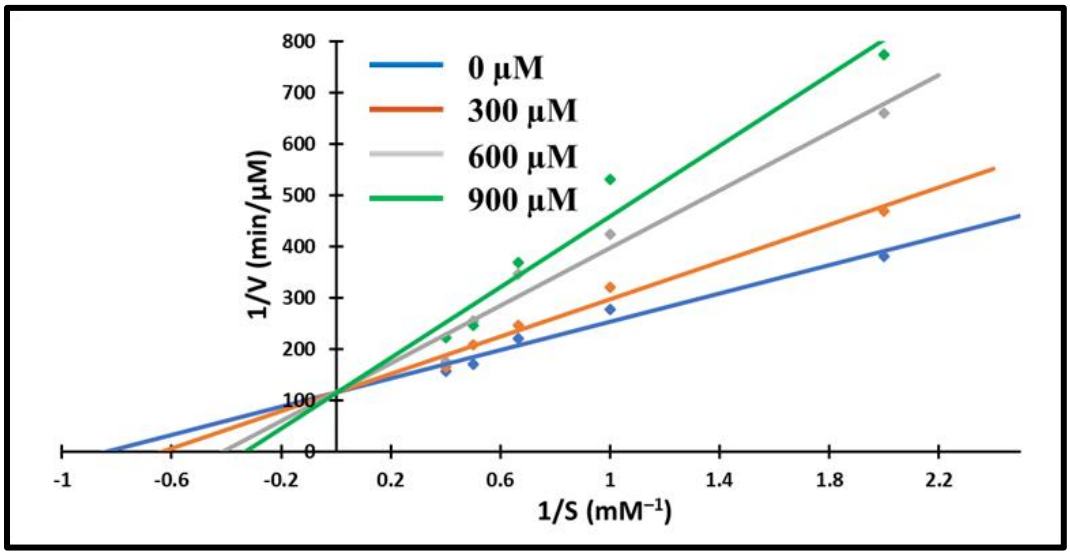

Figure 5.16: Mode of inhibition of α-G by silychristin using Lineweaver Burk plot.

For acarbose and silychristin, the plot shows a typical competitive inhibition pattern, where the slope of the lines increases with higher concentrations of the inhibitor (0 μM, 300 μM, 600 μM, 900 μM), but the lines intersect at the same point on the y-axis. This indicates that acarbose and silychristin compete with the substrate for binding at the α-G enzyme's active site without altering the maximum velocity (Vmax). Silychristin, with a Ki of -227.38 μM, is a more effective inhibitor than acarbose, which has a Ki of -281.48 μM, meaning silychristin requires a lower concentration to inhibit 50% of the enzyme activity compared to acarbose.

For hyperoside, the plot demonstrates a different pattern, indicative of non-competitive inhibition. Unlike acarbose and silychristin, the lines in the hyperoside plot do not intersect at the same point on the y-axis. This suggests that hyperoside binds to a site other than the active site on the enzyme, reducing the α-G enzyme's overall activity regardless of the substrate concentration. The Ki value for hyperoside is -166.67 μM, making it the most potent inhibitor among the three, as it requires the lowest concentration to inhibit 50% of the α-G enzyme's activity.

5.4.5 Cell line study

5.4.5.1 Cell Differentiation

Figure 5.17. A and Figure 5.17. B represents distinct stages in the development of 3T3-L1 cells, transitioning from preadipocytes to mature adipocytes through a process of differentiation. Initially, the 3T3-L1 cells are in the preadipocyte stage, characterized by their spindle-shaped, fibroblast-like appearance. At this stage, the cells have a centrally located nucleus and are elongated. These undifferentiated preadipocytes lack significant metabolic activity related to glucose or lipid storage and do not respond to insulin. This is reflected in the minimal expression of GLUT-4 transporters, which play a crucial role in insulin-stimulated glucose uptake.

In Figure 5.17. B, the 3T3-L1 cells have undergone differentiation into mature adipocytes. This transition is marked by a significant morphological change, where the cells become more rounded and accumulate lipid droplets in the cytoplasm. These lipid droplets are a hallmark of adipocytes and represent their role in lipid and fatty acid storage. Furthermore, mature adipocytes are highly involved in insulin signaling due to the increased presence of GLUT-4 transporters on their membrane. This enables enhanced glucose uptake in response to insulin. The differentiated adipocytes also demonstrate higher metabolic activity, actively participating in lipid synthesis and fatty acid metabolism, storing triglycerides, and playing a vital role in maintaining glucose homeostasis. The comparison between these two stages highlights the functional transition from low metabolic activity in preadipocytes to high insulin responsiveness and glucose uptake in mature adipocytes, emphasizing the importance of the 3T3-L1 cell line as a model for studying adipogenesis, insulin resistance, and metabolic diseases like obesity and diabetes.

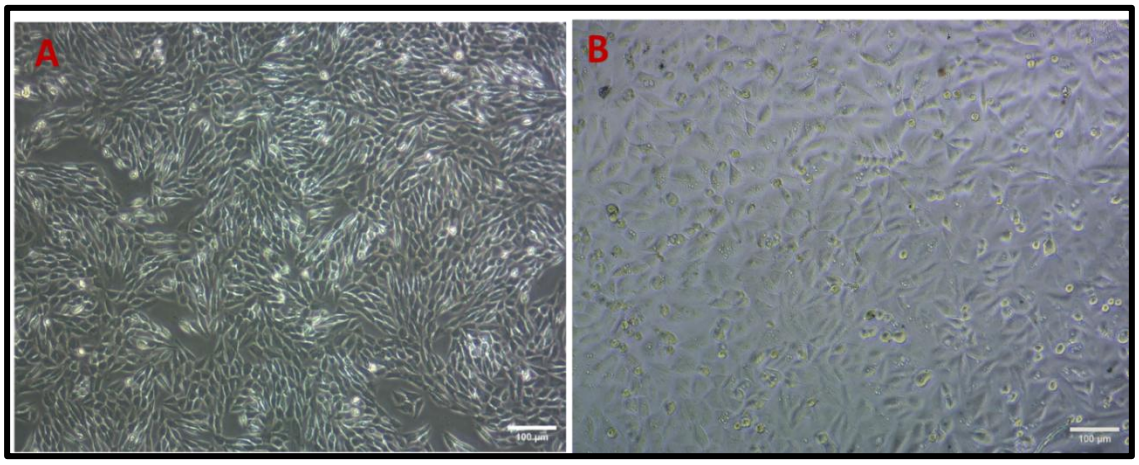

Figure 5.17: 3T3-L1 preadipocytes, displaying spindle-shaped morphology before differentiation (Figure A), and fully differentiated 3T3-L1 adipocytes after exposure to differentiation medium, characterized by a rounded shape and accumulation of lipid droplets, indicating successful adipogenesis (Figure B).

5.4.5.2 Cytotoxicity Study

The cytotoxicity of silychristin and hyperoside on the 3T3-L1 cell line was assessed after 24 hours of treatment across a range of concentrations (6.25–200 μg/mL). Both compounds exhibited a concentration-dependent decline in cell viability, as shown in Figure 5.18.A and Figure 5.18.B. For silychristin, cell viability remained relatively stable at lower concentrations (6.25–25 μg/mL), with only a slight reduction compared to the untreated control. However, a notable decline in cell viability was observed at concentrations of 50 μg/mL and higher, with near-complete cytotoxicity at 200 μg/mL. The IC_{50} for silychristin was 129.66 μg/mL, indicating that at this concentration, 50% of the cells remained viable after 24 hours. In contrast, hyperoside demonstrated a more pronounced cytotoxic effect. Minimal impact on cell viability was seen at lower concentrations (up to 12.5 μg/mL), but a significant reduction occurred at concentrations of 25 μg/mL and higher. At 200 μg/mL, cell viability was nearly completely lost. The IC_{50} for hyperoside was determined to be 40.60 μg/mL, suggesting that hyperoside is more potent than silychristin, as a lower concentration is required to reduce cell viability by 50%.

These findings indicate that both silychristin and hyperoside exhibit cytotoxic effects on 3T3-L1 cells, with hyperoside showing a significantly higher potency. This difference in cytotoxicity could have important implications for future studies exploring the therapeutic potential of these compounds, particularly in targeting diseases related to cell proliferation and metabolic disorders.

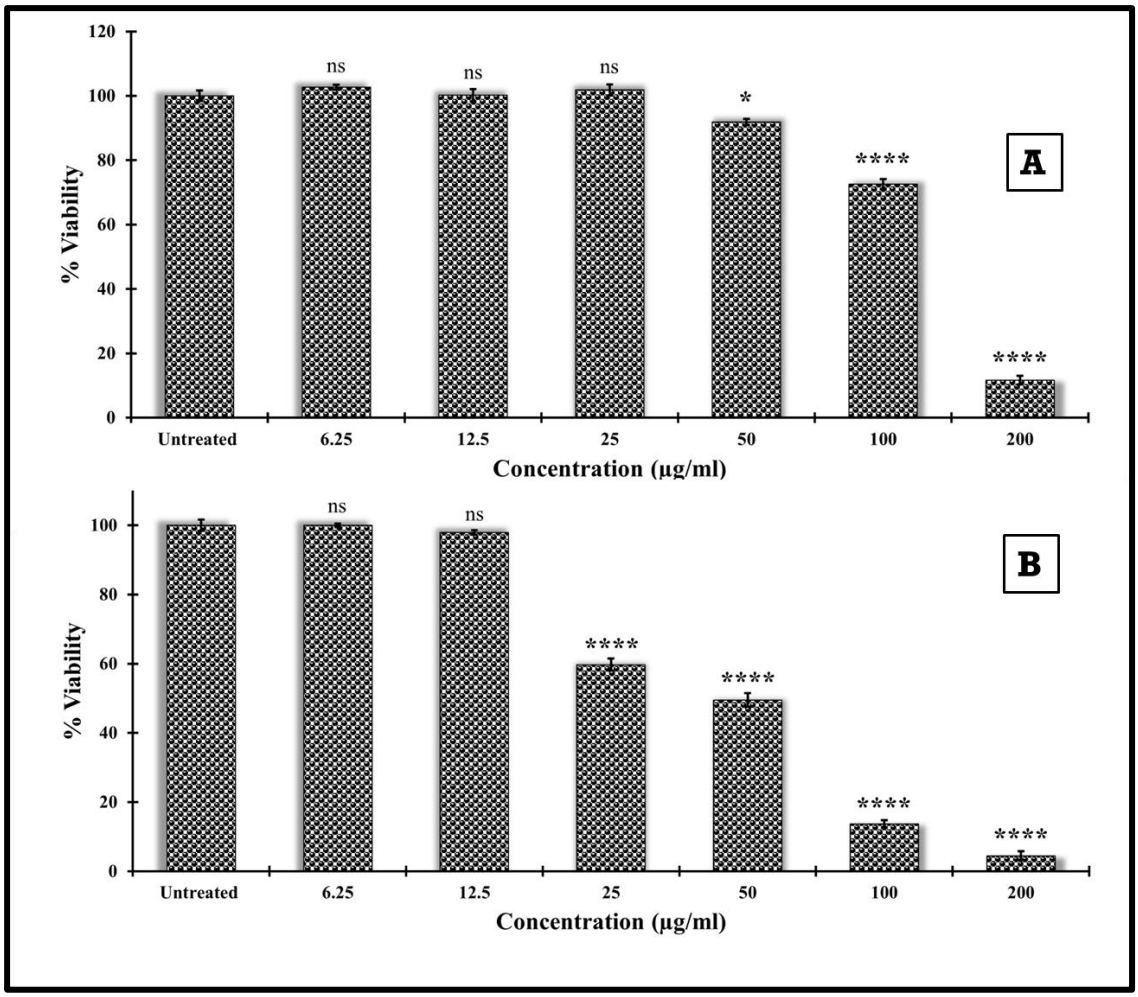

Figure 5.18: Percentage viability of 3T3-L1 cells after 24-hour treatment with silychristin (Figure A) and hyperoside (Figure B). Untreated = vehicle control (set to ~100%). Bars show mean ± SD; n = 3 independent experiments per concentration. Statistics were performed in GraphPad Prism using one-way ANOVA within each compound, followed by Dunnett's multiple-comparisons test vs the untreated control. Significance: $P < 0.05$ (*), $P < 0.01$ (**), $P < 0.001$ (***), $P < 0.0001$ (****); ns = not significant ($P = NS$) (two-tailed, $\alpha = 0.05$).

5.4.5.3 Glucose Uptake Assay

Figure 5.19 presents histograms from the invitro 2-NBDG glucose uptake assay, which illustrates the glucose uptake by 3T3-L1 cells treated with silychristin and hyperoside, compared to untreated control cells. The X-axis indicates the amount of 2-NBDG, a fluorescent glucose analog taken up by the cells, and the Y-axis shows the number of cells. Cells were treated for 24 hours with 12.5 µg/mL silychristin and 6.25 µg/mL hyperoside, concentrations that did not show any cytotoxic effects in prior studies.

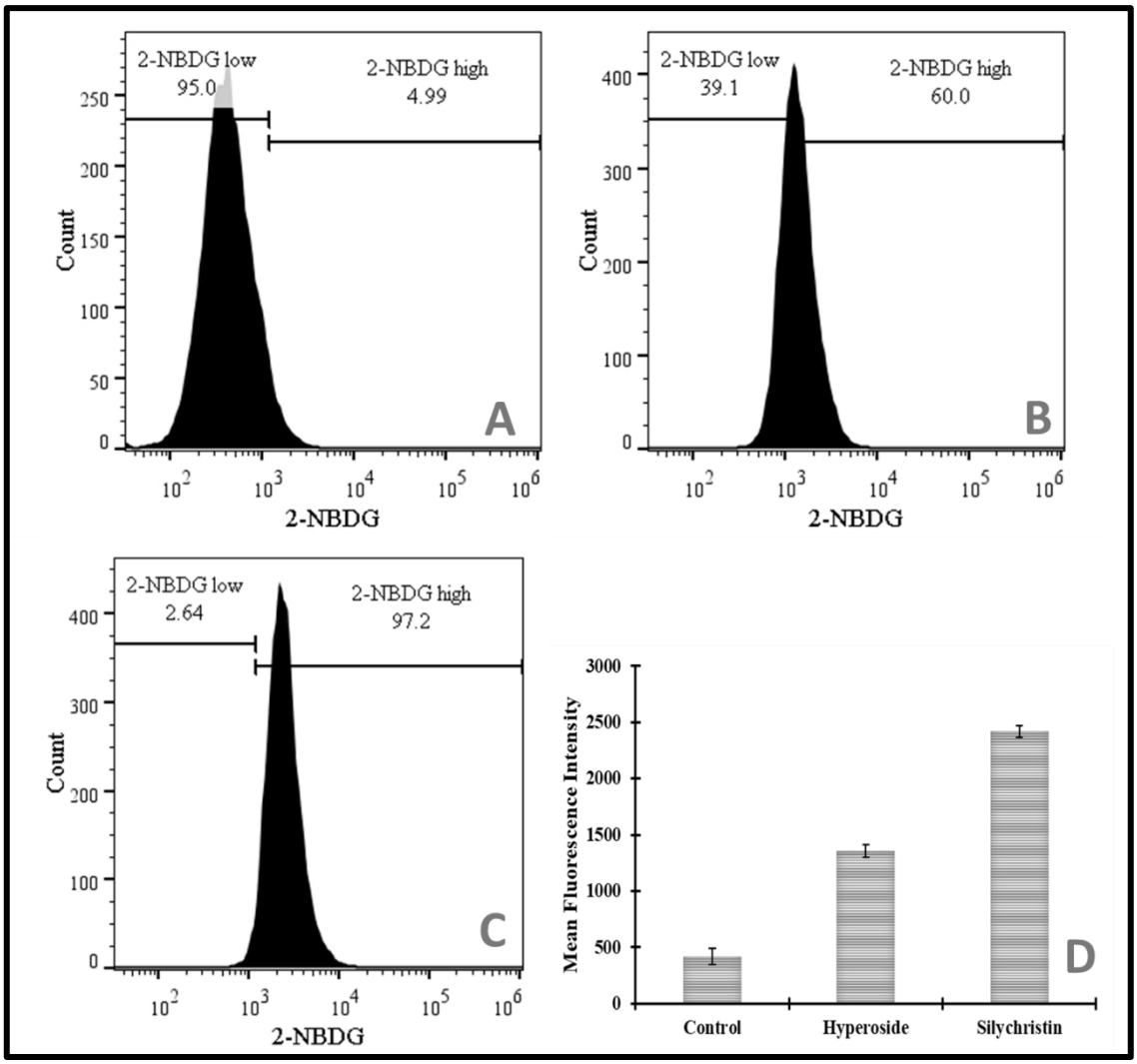

Figure 5.19: 2-NBDG glucose uptake assay on 3T3-L1 cells. (A) Untreated control cells; (B) Cells treated with hyperoside; (C) Cells treated with silychristin; (D) Bar graph representing the mean fluorescence intensity (MFI) of 2-NBDG uptake, where both hyperoside and silychristin treatments significantly increase glucose uptake compared to the control, with silychristin showing the greatest effect.

2-NBDG glucose uptake assay does not involve antibodies but uses a fluorescent glucose analog taken up via glucose transporters. Therefore, an isotype control is not applicable here. Isotype controls are used in antibody-based flow cytometry to account for nonspecific antibody binding and background fluorescence signals (Maecker and Trotter, 2006). In this assay, untreated cells incubated with 2-NBDG alone serve as the appropriate baseline control to measure specific glucose uptake, ensuring that changes in fluorescence reflect metabolic activity rather than nonspecific probe interactions. Thus,

the untreated 2-NBDG-treated group effectively functions as the control for this functional metabolic assay.

In the control group (figure 5.19.A), 95% of the cells exhibited low glucose uptake, with only 4.99% displaying high uptake. Following treatment with hyperoside (figure 5.19.B), there was a clear shift toward higher glucose uptake, with 60% of cells showing increased 2-NBDG uptake, reflecting a noticeable improvement in glucose metabolism. However, 39.1% of cells remained in the low uptake category, suggesting a moderate effect of hyperoside on glucose metabolism. In contrast, treatment with silychristin (figure 5.19.C) resulted in a more significant enhancement in glucose uptake, with 97.2% of the cells exhibiting high glucose uptake and only 2.64% showing low uptake. This highlights that silychristin had a more potent effect on glucose uptake compared to hyperoside.

Figure 5.19.D quantifies the results by showing the Mean Fluorescence Intensity (MFI), representing the average 2-NBDG uptake per cell. Higher MFI values indicate higher glucose uptake and It is used to calculate fold change in glucose uptake. The data reveal that hyperoside and silychristin enhanced glucose uptake by 3.2-fold and 5.7-fold, respectively, compared to the control group, with silychristin exhibiting greater potency in promoting glucose uptake compared to hyperoside. These findings suggest that both silychristin and hyperoside can promote glucose uptake in adipocytes, with silychristin demonstrating a stronger and more widespread impact.

The enhanced glucose uptake by silychristin than hyperoside was due to their distinct structural and physicochemical properties, which influence cellular permeability and mechanisms of action. Silychristin is a non-glycosylated flavonolignan with higher lipophilicity, facilitating passive diffusion across adipocyte membranes, such as in 3T3-L1 cells. This enhanced membrane permeability allows efficient intracellular access,

enabling silychristin to modulate key signaling pathways, notably PI3K/Akt and AMP-activated protein kinase (AMPK) that regulate GLUT4 translocation and glucose uptake (Mi et al., 2022).

Pharmacologically, silychristin has been shown to significantly lower blood glucose, enhance insulin secretion, and improve pancreatic β-cell structure and function in diabetic models (Qin et al., 2017). Mechanistic studies indicate activation of antioxidative and cytoprotective pathways such as Nrf2-HO-1/SOD2 along with modulation of estrogen receptor α, which collectively confer β-cell protection and improved glucose homeostasis (Wang et al., 2020). Molecular docking simulations further suggest silychristin's ability to interact directly with the insulin receptor, enhancing downstream insulin signaling and glucose uptake (Pferschy-Wenzig et al., 2014).

Conversely, hyperoside is a hydrophilic glycosylated flavonoid whose sugar moiety reduces membrane permeability, limiting passive diffusion into cells. Its cellular uptake often depends on active transport mechanisms or enzymatic deglycosylation, processes that may be inefficient or absent in vitro (Wen and Walle, 2006). Additionally, hyperoside is considered a prodrug requiring in vivo conversion to its aglycone form, quercetin, for full biological activity (Manach et al., 2005). These factors likely contribute to the comparatively lower glucose uptake enhancement observed in cell culture models. Mechanistically, hyperoside exhibits its effects primarily by inhibiting cell proliferation and reducing high glucose-induced cellular stress via suppression of the ERK/CREB/miRNA-34a signaling pathway, a route more involved in cytoprotection rather than direct stimulation of insulin-mediated glucose transport (L. Zhang et al., 2020). This increased glucose uptake highlights the potential for these compounds in improving insulin sensitivity and managing metabolic disorders, such as diabetes.

5.4.5.4 Wound Healing Assay

Figure 5.20 illustrates the results of a scratch wound healing assay conducted on 3T3-L1 adipocytes over a period of 48 hours. The assay was used to evaluate cell migration and wound closure in cells treated with 12.5 µg/mL silychristin and 6.25 µg/mL hyperoside, with untreated cells serving as controls. The progression of wound closure was observed at 0 hours, 24 hours, and 48 hours to assess the effects of these treatments on wound healing.

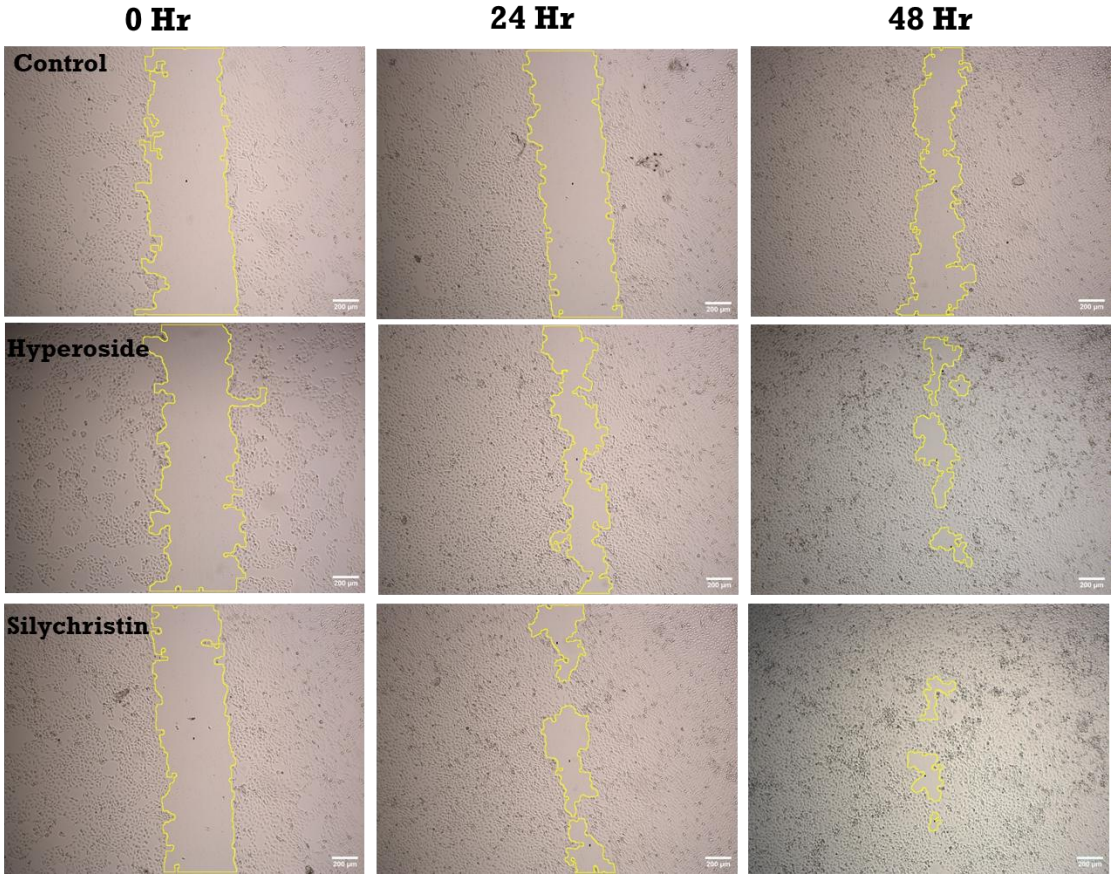

Figure 5.20: Invitro scratch wound healing assay of 3T3L1 cells at 0, 24, and 48 hours post-treatment with hyperoside and silychristin, compared to untreated control cells. Yellow outlines highlight the wound area at each time point, showing cell migration and wound closure over time. Scale bar: 200 µm.

In the control group, the cells did not receive any treatment, and at 0 hours, a distinct wound can be observed. Over the course of 24 hours, there was minimal closure of the wound, and by 48 hours, only slight cell migration had occurred, indicating limited wound

healing without treatment. The slow progression of closure in the control suggests that natural cell migration is insufficient to achieve significant wound healing within this time frame. Cells treated with 6.25 µg/mL hyperoside displayed a more favourable response. At 24 hours, a clear reduction in the wound area was visible, indicating that hyperoside promotes cell migration and wound closure more effectively than in the untreated group. By 48 hours, the wound had significantly closed, with only small gaps remaining, demonstrating that hyperoside enhances the wound healing process compared to the control. Cells treated with 12.5 µg/mL silychristin revealed a more pronounced reduction in the wound area even at 24 hours than the hyperoside treated group. By 48 hours, the wound was almost completely closed, indicating that silychristin has more pronounced effects on promoting cell migration and wound closure than both hyperoside and the untreated control group.

Figure 5.21, the bar graph shows the percentage of wound healing at 24 hours and 48 hours in the scratch wound healing assay performed on 3T3-L1 adipocytes. The wound healing capacity of untreated (control) cells and cells treated with 6.25 µg/mL hyperoside and 12.5 µg/mL silychristin was evaluated by measuring the percentage of wound closure over time. At 24 hours, the control group exhibited minimal wound healing, with around 20% closure. In contrast, the cells treated with hyperoside showed a much higher healing rate, reaching approximately 60%, while silychristin-treated cells exhibited the most pronounced wound closure at about 70%. This indicates that both hyperoside and silychristin effectively promoted cell migration and wound healing, with silychristin being more effective than hyperoside at this time point.

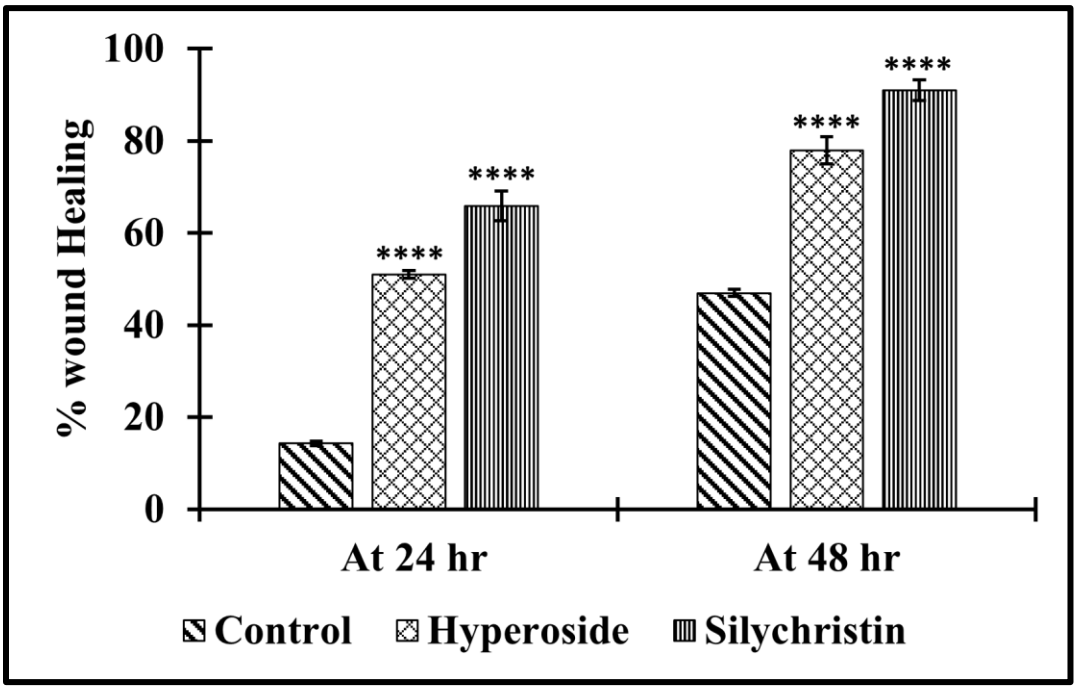

Figure 5.21: Percentage of wound healing at 24 and 48 hours for control, hyperoside, and silychristin-treated 3T3L1 cells. Bars show mean ± SD; n = 3 independent experiments per group and time point. Statistics were performed in GraphPad Prism using a two-way ANOVA (factors: treatment × time) followed by Tukey's multiple-comparisons test. Asterisks denote differences vs control at the same time point; Significance: $P < 0.05$ (*), $P < 0.01$ (**), $P < 0.001$ (***), $P < 0.0001$ (****); ns = not significant ($P = NS$) (two-tailed, $\alpha = 0.05$).

By 48 hours, the control group had improved to about 45% wound closure, but both treated groups showed significantly higher rates of healing. Hyperoside-treated cells achieved around 75% wound closure, while silychristin-treated cells exhibited nearly 90% wound closure, indicating that silychristin continued to be the most effective in promoting wound healing. Thus, both silychristin and hyperoside enhance wound healing in 3T3-L1 adipocytes, with silychristin showing the most potent effect. These findings suggest that these compounds could potentially be used to promote tissue repair and wound healing.

5.4.6 Computational Study

5.4.6.1 Molecular Docking

Molecular docking is a widely utilized technique in structure-based drug design that allows the assessment of ligand binding conformation on its binding site (Gao et al.,

2022; Mengist et al., 2021; Patel et al., 2022). Docking was performed to elucidate the inhibitory ability of isolated phytochemicals hyperoside and silychristin against essential carbohydrates hydrolysing enzymes α-A and α-G. The BE, and hydrogen and hydrophobic interactions of hyperoside and silychristin and standard drug acarbose with α-A and α-G protein have been represented in Table 5.3.

Table 5.3: Molecular docking interactions of Acarbose, Hyperoside, and Silychristin with α-A and α-G, showing varying binding affinities, and key residues involved in hydrogen bonding and hydrophobic interactions.

S. No	Ligand Name	Binding Energy (Kcal/mol)	Hydrogen Bond Amino Acids	Hydrophobic interactions Amino Acids
1	Acarbose (α-A)	-4.71	Glu 240, Glu 233, Arg 195, His 201	Ala 307, Tyr 151, Trp 58, Ile 235, Leu 237, Ala 198, Ile 162, Lys 200, Asp 197, Asp 236, Asp 300, His 299, His 305, His 101, Gly 238
2	Hyperoside (α-A)	-6.65	Glu 240, His 305, Lys 200	Leu 237, Ile 235, Val 234, Tyr 151, Ala 307, Ala 190, Gly 306, Asp 300, His 201, Glu 233, Ser 190
3	Silychristin (α-A)	-8.98	Gln 63, His 299, Ala 106, Trp 59	Glu 60, Asp 300, Trp 58, Tyr 62, Gly 104, Gly 164, Asn 105, Glu 233, Arg 195, Asp 197, Leu 162, Thr 163, Val 107, Leu 164
4	Acarbose (α-G)	-4.36	Gln 603, Asp 542, Asp 327	Trp 441, Ile 326, Ile 361, Trp 299, Tyr 605, Trp 406, Phe 450, Phe 575, His 600, Arg 334, Arg 526, Asp 203, Asp 443, Met 444
5	Hyperoside (α-G)	-7.25	Asp 542, Asp 203, His 600, Asp 327	Gln 603, Ser 446, Trp 441, Ile 326, Ile 364, Trp 299, Tyr 605, Trp 405, Phe 450, Phe 575, Arg 334, Arg 526, Asp 443, Met 444, Asp 571
6	Silychristin (α-G)	-6.91	Asp 542, Asp 327, Asp 203	Ile 328, Asp 443, Ile 864, Ile 326, Trp 441, Trp 406, Trp 299, Phe 575, Phe 539, Phe 450, Val 451, Gly 541, Arg 526, Arg 580, Asn 449, Ser 448, Lys 480, His 600

5.4.6.1.1 α-Amylase

The docking results demonstrated that acarbose formed five hydrogen bond interactions with residue of α-A. These findings are consistent with the docking results reported by Chigurupati et al. (Chigurupati et al., 2021b). The 2D molecular docking interactions between the hyperoside and silychristin and standard drug acarbose with α-A proteins have been illustrated in Figure 5.22.

Based on the previous study, it has become evident that Asp197, Glu233, Asp300, Arg195, Asn298, Arg337, Asn100, Arg158, Asp167, and His201 are active site residues

of α-A protein (Brayer et al., 2000, 1995). Among them, the catalytic triad residues, Asp197, Glu233, and Asp300, function cooperatively as nucleophiles, acid/base catalysts, and transition state stabilizers to cleave the glycosidic bond in starch (Marengo et al., 2022).

Acarbose, an oligosaccharide, has a BE of -4.71 kcal/mol, which reflects the moderate strength of its interaction with α-A. Acarbose forms crucial hydrogen bonds with the carboxylate side chains of Glu240 and Glu233. The hydroxyl groups (-OH) on acarbose donate hydrogen atoms to the negatively charged oxygen atoms of these carboxylate groups. These interactions are key to stabilizing acarbose within the enzyme's active site, effectively blocking the enzyme's natural substrate. Additionally, acarbose engages with the guanidinium group of Arg195 through hydrogen bonding. This interaction involves the polar attraction between the oxygen atoms of acarbose's hydroxyl groups and the positively charged guanidinium group. The imidazole ring of His201 also acts as a hydrogen bond donor, interacting with the hydroxyl groups of acarbose and helping to secure it in an orientation that inhibits enzyme activity. Alongside hydrogen bonding, acarbose interacts hydrophobically with residues like Ala307 and Ile235. These hydrophobic amino acids engage with the glycosidic backbone of acarbose, fitting into the enzyme's nonpolar pockets. This positioning reduces the solvation energy and adds to the overall stability of the acarbose-α-A complex. Another interaction occurs with Trp58, where the aromatic ring of Trp58 interacts with acarbose via van der Waals forces.

Hyperoside, a flavonoid glycoside with a quercetin core and a sugar moiety, exhibits a BE of -6.65 kcal/mol, indicating a stronger and more stable interaction with α-A compared to acarbose. One of the key interactions involves Glu240, where the hydroxyl groups on the sugar moiety of hyperoside donate hydrogen atoms to the carboxylate oxygens of Glu240.

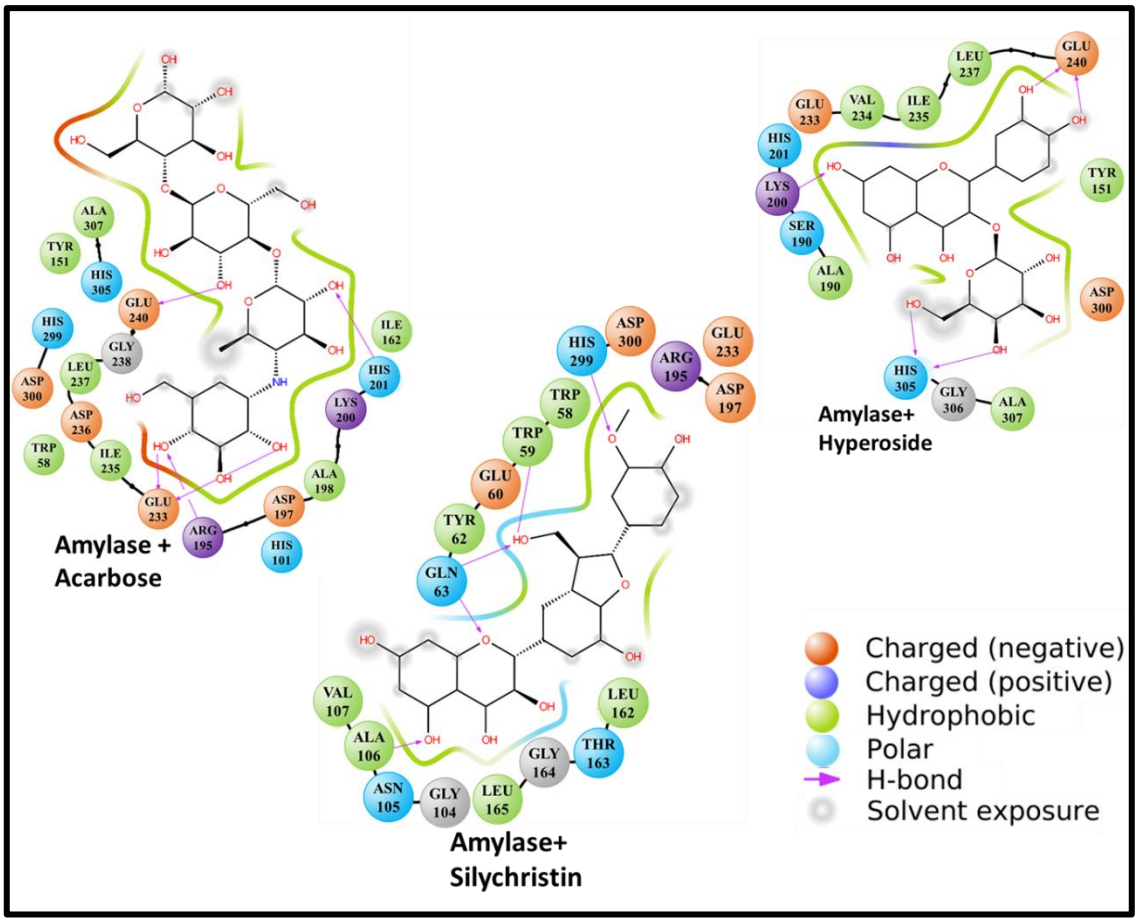

Figure 5.22: 2D plots showing molecular interaction between binding-site residues of α-A protein with ligands.

This hydrogen bond is crucial for anchoring hyperoside within the binding site of enzyme, thereby blocking the processing of the enzyme's natural substrate. Additionally, hyperoside forms a hydrogen bond with the imidazole side chain of His305. The hydroxyl groups on the quercetin ring interact with HIS305, securing hyperoside in the proper orientation within the binding pocket and enhancing the stability of the complex. Another significant hydrogen bond occurs with Lys200, where the positively charged ammonium group forms a strong hydrogen bond with the oxygen atoms of hyperoside's hydroxyl groups, further contributing to the stability of the enzyme-ligand complex. Moreover, residues like Ile235 and Val234 contribute to hydrophobic contacts with the less polar regions of hyperoside, such as its aromatic rings. These hydrophobic interactions further

anchor hyperoside within the enzyme's hydrophobic pocket, ensuring a secure fit that inhibits enzyme activity.

The flavonolignan silychristin has the strongest and most consistent interaction with α-A, as evidenced by its highest negative BE of -8.98 kcal/mol. It created strong hydrophobic and hydrogen bonding contacts inside the enzyme's binding site. Silychristin establishes an interaction with the amide side chain of Gln63, one of the important hydrogen bond interactions. The carbonyl oxygen of Gln63 acts as a hydrogen bond acceptor, interacting with the hydroxyl groups of silychristin, thus stabilizing the ligand within the enzyme's binding pocket. Gly106 created a crucial interaction in which one of the -OH groups of silychristin was hydrogen-bonded to the backbone amide of Gly106. Furthermore, silychristin interacts with the indole side chain of Trp59 through hydrogen bonds. The N-atom in the indole ring forms hydrogen bonds with the hydroxyl groups on silychristin, adding further stability to the enzyme-ligand complex. Moreover, silychristin forms a hydrogen bond with the imidazole ring of His299, where the nitrogen atoms act as hydrogen bond donors, effectively locking the ligand in place. Besides these hydrogen bonds, silychristin engages in significant hydrophobic interactions, particularly with residues like Val107 and Leu162. The hydrophobic regions of silychristin, including its aromatic rings, interact with the nonpolar side chains of these residues, helping to orient the ligand within the enzyme's active site. These hydrophobic interactions reduce the desolvation penalty, thereby increasing the binding affinity.

5.4.6.1.2 α-Glucosidase

The 2D molecular docking interactions between the hyperoside and silychristin and standard drug acarbose with α-G proteins have been illustrated in Figure 5.23. For α-G, residue Asp443 acts as catalytic nucleophiles; Asp542 behaves like acid/base catalyst and His600, Asp327, Arg526, Asp203, Trp406, Phe450 are substrate binding residues

(Bharathi et al., 2014; Sim et al., 2010, 2008). Acarbose has a BE of -4.36 kcal/mol, indicating a moderate binding affinity with α-G. It has multiple hydroxyl (-OH) groups attached to its sugar moiety, which are crucial for forming hydrogen bonds with specific residues in the enzyme. One such interaction involves the hydroxyl group on one of the sugar rings forming a direct hydrogen bond with the carboxylate side chain of Asp327. In this connection, the hydroxyl oxygen atom of acarbose acts as a hydrogen donor, while the carboxylate oxygen of Asp327 serves as an acceptor, anchoring acarbose within the enzyme's active site. Another significant hydrogen bond forms between a hydroxyl group on a different sugar ring of acarbose and the carboxylate group of Asp542. This interaction stabilizes the ligand within the binding pocket, as the acidic nature of Asp542 provides a polar interaction point for acarbose, with the hydroxyl group acting as a donor.

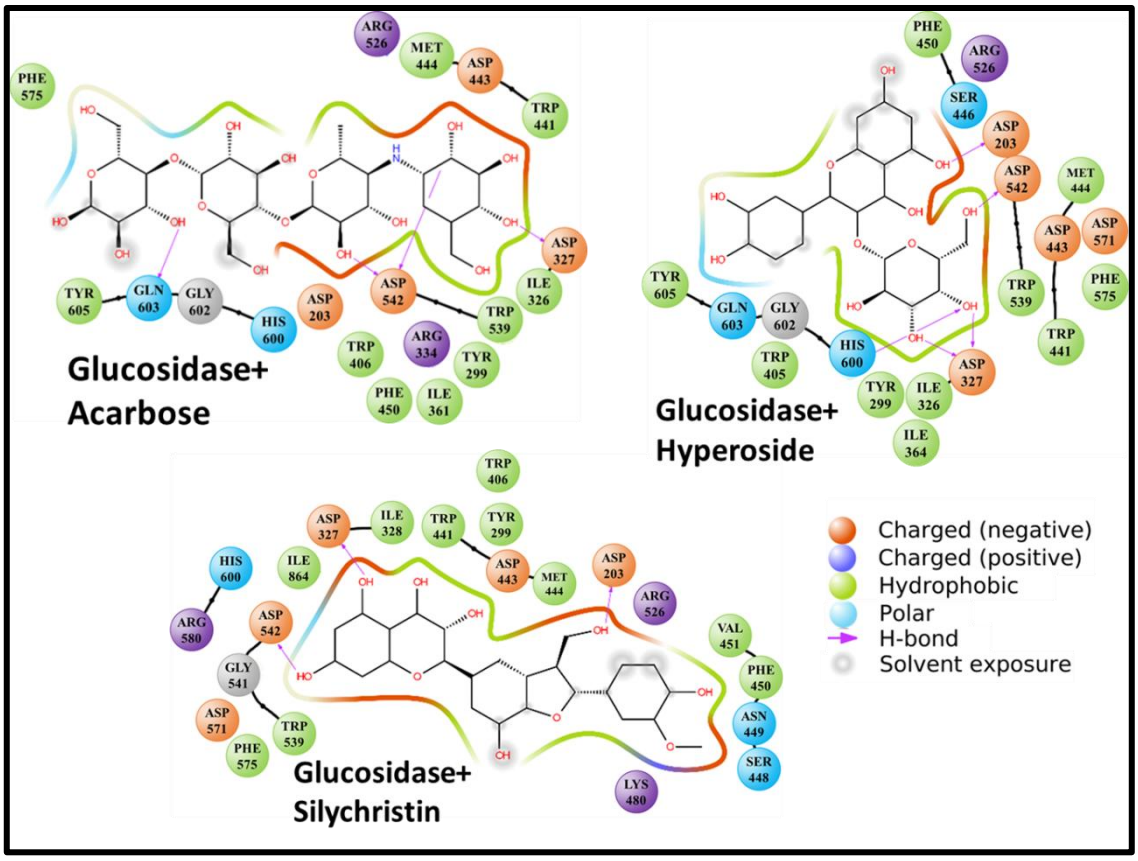

Figure 5.23: 2D plots showing molecular interaction between binding-site residues of α-G protein with ligands.

Beyond hydrogen bonding, acarbose engages in hydrophobic interactions with residues such as Trp 441, Ile 326, and Ile 361. The indole ring of Trp 441 interacts with the hydrophobic face of acarbose's sugar rings through van der Waals forces, where the aromatic ring system of Trp 441 stacks against the non-polar face of acarbose's sugar moiety. This stacking interaction contributes to the overall binding by creating a snug fit within the enzyme's active site. Additionally, the aliphatic side chains of Ile 326 and Ile 361 make contact with the non-polar regions of acarbose, specifically the methylene groups within the sugar rings.

Hyperoside demonstrates a significantly higher binding affinity with α-G, with a BE of -7.25 kcal/mol. Hyperoside contains multiple phenolic hydroxyl (-OH) groups on its flavonoid core, which are key players in hydrogen bonding. One stable interaction occurs when the -OH group located on the hyperoside's C-ring creates a hydrogen bond with Asp 542's carboxylate side chain. This bond is complemented by another interaction where the sugar moiety of hyperoside (glucoside part) contains several hydroxyl groups. One of these groups forms a hydrogen bond with the carboxylate group of Asp 203. This interaction is vital as the hydroxyl group of the sugar moiety donates a hydrogen atom to the carboxylate of Asp 203. Additionally, the aromatic ring of His 600 made hydrogen bond with the hydroxyl groups on the flavonoid core of hyperoside. The N- atom in the imidazole ring of His 600 acts as a hydrogen bond acceptor, forming a relatively stable interaction with the phenolic -OH group of hyperoside. Hyperoside also forms a hydrogen bond with Asp 327, similar to acarbose, through -OH groups of sugar moiety of hyperoside combined with the carboxylate group of Asp 327, adding to the ligand's anchoring within the enzyme's binding site. The hydrophobic surfaces of Ile 326 and Ile 364 interact with the non-polar regions of hyperoside, especially the aromatic system, enhancing the interaction network. Interestingly, even residues like Gln 603 and Ser 446,

which are typically polar, participate in hydrophobic interactions with the aromatic rings of hyperoside. Their side chains make contact with the planar ring system of hyperoside, increasing the compound's binding affinity by contributing to a more hydrophobic environment within the binding pocket.

Silychristin exhibits a robust interaction with α-G, with a BE of -6.91 kcal/mol. This affinity is due to multiple hydrogen bonds and hydrophobic interactions facilitated by its complex flavonolignan structure. One such interaction occurs between a phenolic hydroxyl group on silychristin and the carboxylate group of Asp 542. The acidic nature of the phenolic -OH makes it an effective hydrogen donor, resulting in a stable interaction with the negatively charged carboxylate of Asp 542. Another crucial hydrogen bond is formed between a phenolic hydroxyl group on silychristin and the carboxylate group of Asp 203. Here, the hydroxyl group donates a hydrogen atom to the oxygen of the carboxylate, further enhancing the molecule's binding stability. Silychristin also forms a hydrogen bond with Asp 327 through one of its hydroxyl groups, anchoring it within the enzyme's active site and enhancing its inhibitory effect. The hydrophobic interactions of silychristin are noteworthy, involving residues such as Ile 328 and Asp 443. While Asp 443 has polar characteristics, its hydrophobic side chain interacts with the aromatic rings and methoxy groups of silychristin. The bulky aromatic ring system of silychristin provides a large surface area for van der Waals interactions with Ile 328 and Asp 443, promoting a snug fit within the enzyme's binding pocket. Furthermore, the aliphatic side chain of Ile 864 interacts with the non-polar regions of silychristin, contributing to the molecule's high binding affinity.

The molecular docking studies revealed that hyperoside and silychristin show greater binding affinities and more complex interactions with α-A and α-G compared to acarbose, highlighting their potential as potent enzyme inhibitors.

5.4.6.2 Molecular Dynamic Simulation

Molecular docking establishes only a preliminary outcome on protein-ligand interaction, so molecular dynamic simulation must be carried out to clarify the docking results and stability of protein-ligand complexes (Singh et al., 2022). A molecular dynamic study was conducted for 100 ns to determine the stability and dynamics of protein-ligand complexes. RMSD, RMSF, RoG, and SASA were observed as they determined the protein-ligand interactions.

Root Mean Square Deviation (RMSD) assesses the stability and conformational changes of proteins over time. It quantifies the average displacement of a protein's atomic positions from a reference structure, usually the initial frame of the simulation. The structural and conformational alterations of the protein's backbone atom were investigated using RMSD. Lower RMSD values indicate a more stable protein structure, while higher values suggest greater flexibility and conformational variability. Figure 5.24 and 5.25 shows the RMSD profiles of α-A and α-G respectively, over a 100 ns simulation, comparing their apo forms with complexes formed with acarbose, silychristin, and hyperoside.

In their apo states, both enzymes show moderate flexibility, with RMSD values fluctuating between 0.1 and 0.25 nm, reflecting natural conformational changes. When bound to acarbose, the RMSD values are reduced, indicating some stabilization of the enzymes, though notable fluctuations remain, suggesting a moderate level of stabilization. In contrast, silychristin and hyperoside exhibit consistently lower and more stable RMSD profiles throughout the simulation, indicating that they form more stable and rigid complexes with both enzymes. This suggests that silychristin and hyperoside provide greater structural stabilization to α-A and α-G than acarbose, supporting their potential as more potent inhibitors.

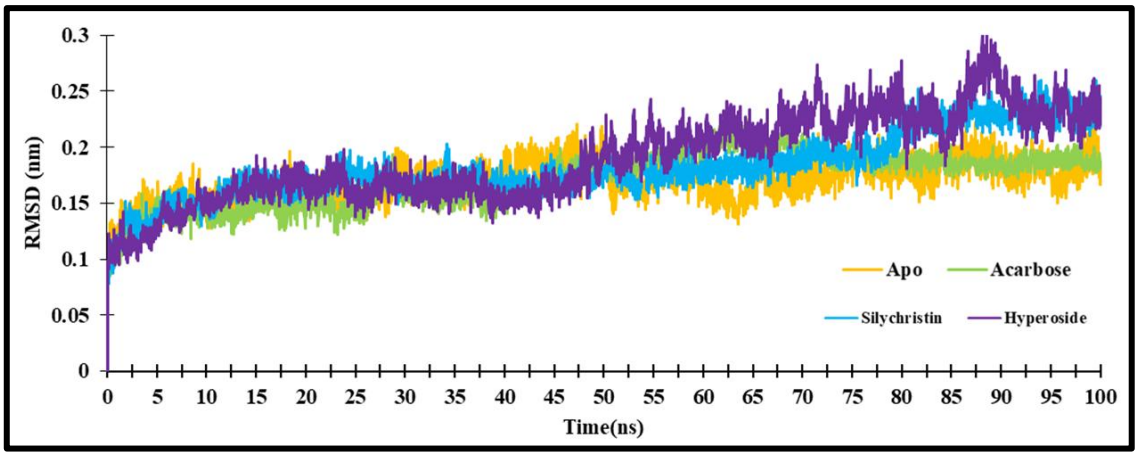

Figure 5.24: RMSD profile of α-A protein in their apo and complex state observed during simulation of 100 ns.

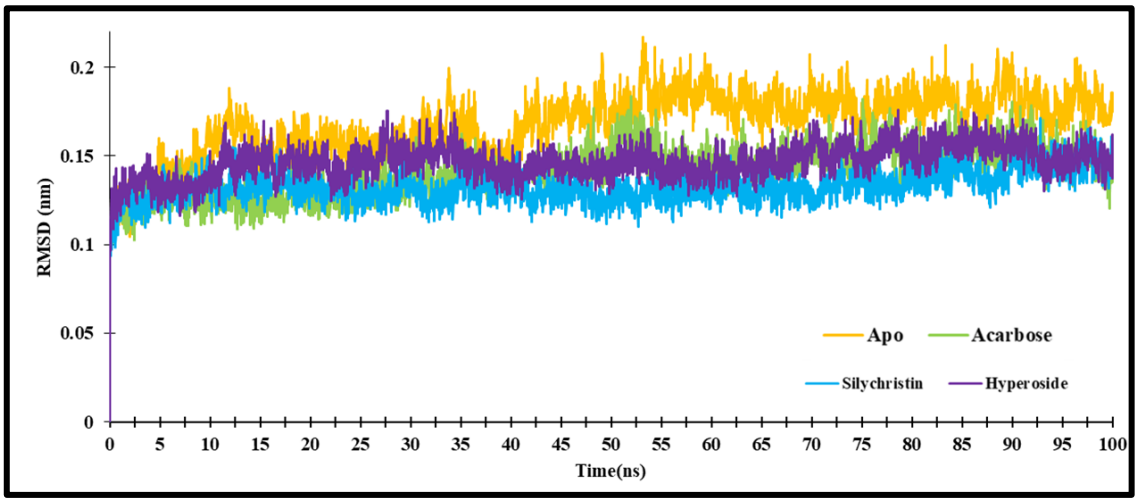

Figure 5.25: RMSD profile of α-G protein in their apo and complex state observed during simulation of 100 ns.

Figures 5.26 and 5.27 illustrate the Root Mean Square Fluctuation (RMSF) profiles of α-A and α-G, respectively, during a 100 ns simulation, comparing their apo forms with their complexes bound to acarbose, silychristin, and hyperoside. RMSF assess the flexibility of individual amino acid residues in a protein over time. It provides insights into which parts of the protein structure are more flexible or more rigid during the simulation. RMSF helps in analyzing the fluctuation of the atom or amino acid residue during the simulation (Singh and Mishra, 2020).

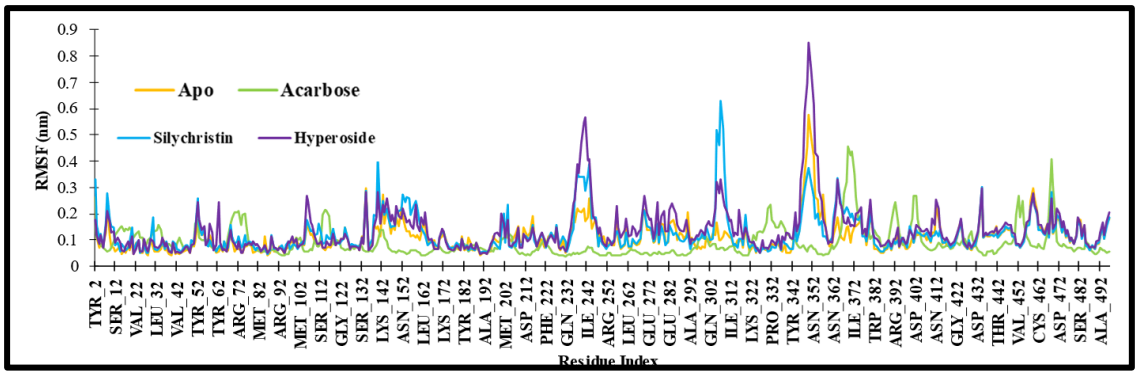

Figure 5.26: RMSF profile of α-A protein in their apo and complex state observed during simulation of 100 ns.

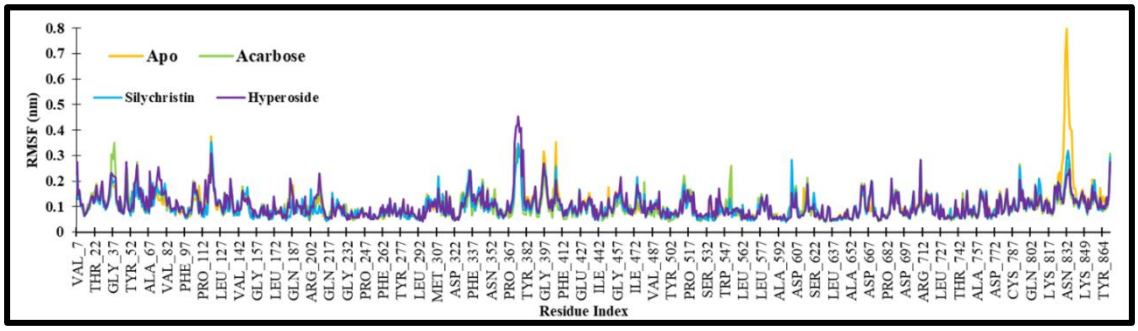

Figure 5.27: RMSF profile of α-G protein in their apo and complex state observed during simulation of 100 ns.

In the apo forms, both enzymes show higher RMSF values, indicating greater flexibility, especially around certain regions such as residues 200-240 and 300-350 in α-A and residues 300-400 in α-G. When acarbose binds to the enzymes, there is a slight reduction in RMSF values, indicating moderate stabilization of specific regions, particularly around the active sites. However, some flexibility remains, suggesting acarbose provides only partial stabilization. In contrast, complexes with silychristin and hyperoside show a more pronounced decrease in RMSF values across the proteins, especially around the active sites and flexible loops. This reduction in fluctuation indicates that silychristin and hyperoside significantly stabilize the enzyme structures, making them more rigid and less prone to conformational changes. Overall, the lower RMSF values in the silychristin and hyperoside complexes indicate more stable interactions with α-A and α-G, supporting their roles as more potent inhibitors compared to acarbose.

Figures 5.28 and 5.29 display the Solvent Accessible Surface Area (SASA) profiles for α-A and α-G, respectively, during simulation. SASA calculates how much of a protein's surface is available to solvent molecules.

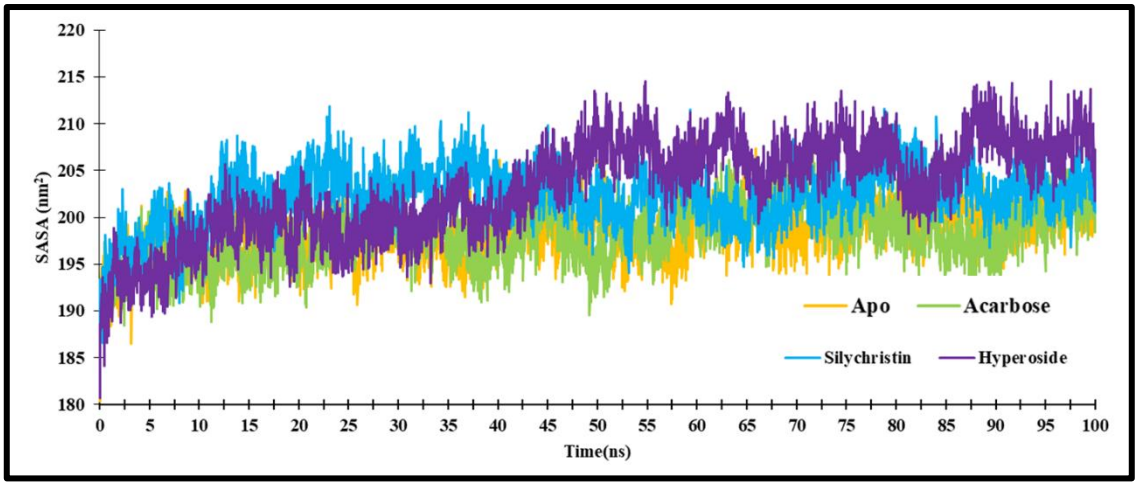

Figure 5.28: SASA value of α-A protein in their apo and complex state observed during simulation of 100 ns.

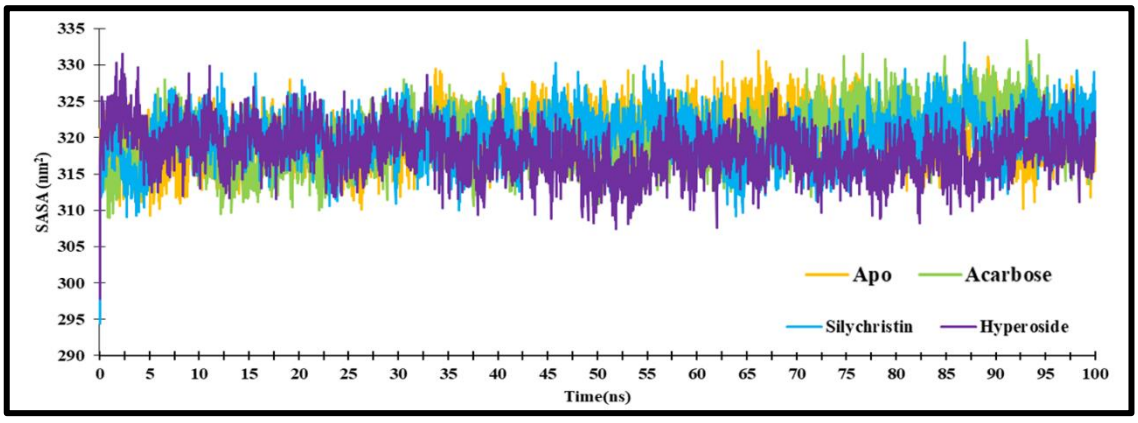

Figure 5.29: SASA value of α-G protein in their apo and complex state observed during simulation of 100 ns.

In their apo forms, α-A shows SASA values fluctuating around 195-205 nm², while α-G ranges between 305-320 nm², indicating natural flexibility and solvent exposure. Binding with acarbose slightly reduces the SASA for both enzymes, with α-A dipping below 200 nm² and α-G falling marginally under 320 nm². This suggests minor conformational changes and moderate stabilization upon acarbose binding. In contrast, silychristin and hyperoside lead to higher SASA values, with α-A reaching up to 210 nm² and α-G around

320-335 nm². These higher values indicate that these inhibitors induce more significant structural rearrangements, increasing surface exposure. This increase suggests that silychristin and hyperoside create stronger interaction networks and potentially more potent inhibition than acarbose.

Figures 5.30 and 5.31 illustrate the Radius of Gyration (RoG) values for α-A and α-G over a 100 ns simulation. The RoG provides a measure of the protein's compactness and overall structural stability, indicating how tightly the protein's mass is packed around its centre of mass. Lower RoG values suggest a more compact structure, while higher values indicate a more expanded conformation.

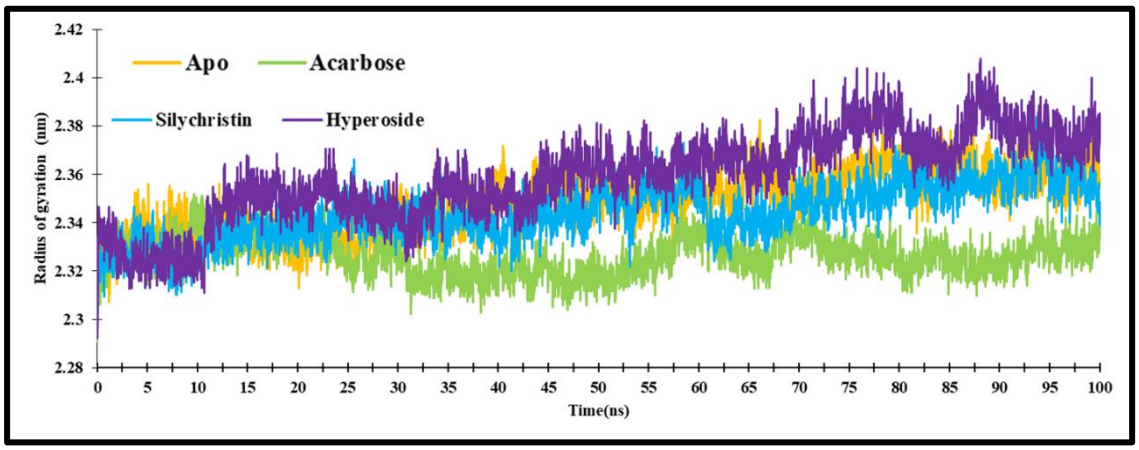

Figure 5.30: RoG value of α-A protein in their apo and complex state was observed during simulation of 100 ns.

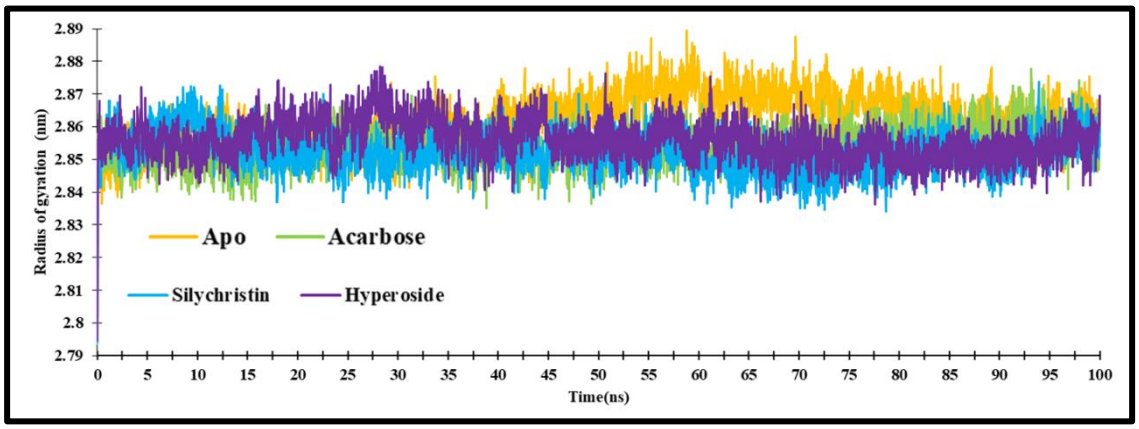

Figure 5.31: RoG value of α-G protein in their apo and complex state observed during simulation of 100 ns.

In the apo forms, α-A fluctuates between 2.32 to 2.36 nm, and α-G ranges from 2.82 to 2.88 nm, reflecting their natural flexibility. Acarbose binding results in a slight decrease in RoG for both enzymes, with α-A around 2.31 to 2.35 nm and α-G around 2.81 to 2.86 nm, suggesting modest compaction and stabilization. In contrast, silychristin and hyperoside show similar or slightly higher RoG values compared to the apo forms.

For α-A, their RoG values fluctuate up to 2.38 nm, and for α-G, they range around 2.82 to 2.89 nm. This indicates that while these inhibitors stabilize the enzymes, they may also induce structural rearrangements rather than simply compacting them. This suggests that silychristin and hyperoside interact with the enzymes, leading to conformational changes, possibly opening binding sites or inducing shifts that contribute to their stronger inhibitory effects.

The number of hydrogen bonds formed between the inhibitors (acarbose, silychristin, and hyperoside) and the enzymes α-A and α-G over a 100 ns simulation has been illustrated in Figure 5.32 and 5.33 respectively. Hydrogen bonds are a key factor in stabilizing enzyme-inhibitor interactions, with a higher number of these bonds typically indicating stronger and more stable binding. Acarbose consistently forms the highest number of hydrogen bonds with both α-A and α-G, fluctuating between 5 to 10 bonds throughout the simulation. This indicates a strong and stable interaction with the enzymes, aligning with its known role as an effective inhibitor. The higher number of hydrogen bonds suggests that acarbose engages extensively with the enzymes' active sites, contributing to its inhibitory potency.

Silychristin and hyperoside form fewer hydrogen bonds with both enzymes, typically ranging between 2 to 5 for silychristin and 2 to 4 for hyperoside. While these numbers are lower than those of acarbose, they still indicate stable interactions. The effectiveness

of silychristin and hyperoside as inhibitors may rely not solely on hydrogen bonding but also on additional interactions such as hydrophobic forces or π-stacking with the enzymes. Despite forming fewer hydrogen bonds, these other stabilizing interactions can contribute to their overall binding affinity and inhibitory potential.

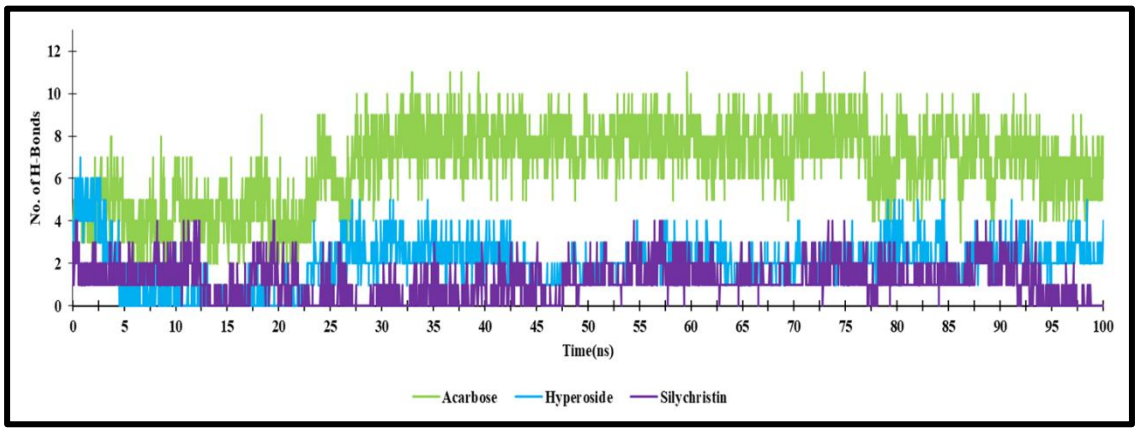

Figure 5.32: Hydrogen bond pattern of α-A protein complexes with Acarbose, Hyperoside and Silychristin observed during simulation of 100 ns.

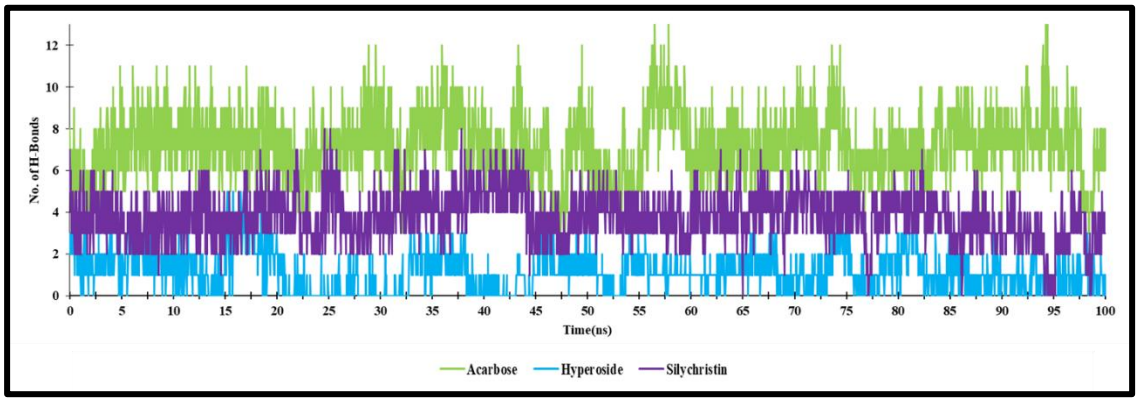

Figure 5.33: Hydrogen bond pattern of α-G protein complexes with Acarbose, Hyperoside and Silychristin observed during simulation of 100 ns.

5.4.6.3 MM/GBSA Calculation

Table 5.4. represents the Molecular Mechanics/Generalized Born Surface Area (MM/GBSA) estimates of binding free energy components for acarbose, hyperoside, and silychristin interacting with α-A and α-G. For α-A, the binding free energy analysis reveals distinct profiles for each inhibitor. Acarbose has a strong binding affinity with a total binding free energy (ΔTOTAL) of -40.80 kcal/mol. This binding strength is driven

mainly by favorable van der Waals interactions (-40.80 kcal/mol) and strong electrostatic interactions (-131.86 kcal/mol), leading to a relatively strong and stable interaction with α-A. Hyperoside shows a more moderate binding affinity for α-A, with total free energy (ΔTOTAL) of -25.44 kcal/mol. It demonstrates moderate van der Waals interactions (-25.82 kcal/mol) and weaker electrostatic interactions (-43.03 kcal/mol) compared to acarbose. As a result, while hyperoside binds less tightly than acarbose, it still interacts favourably with the enzyme, reflecting a stable but not overly strong binding. Silychristin exhibits the strongest binding affinity with α-A, having total free energy (ΔTOTAL) of -48.55 kcal/mol. This is primarily due to very strong electrostatic interactions (-205.98 kcal/mol) and significant van der Waals interactions (-36.52 kcal/mol). These interactions suggest that silychristin forms a particularly stable and robust complex with α-A, making it the most potent inhibitor among the three for this enzyme.

Table 5.4: MM/GBSA estimates of the binding free energy (Kcal/mol).

Complex Name	VDWAALS	EEL	EGB	ESURF	ΔG_GAS	ΔG_SOLV	ΔG_TOTAL
α-A							
Acarbose	-40.8	-131.86	137.11	-5.37	-172.53	131.73	-40.8
Hyperoside	-25.82	-43.03	48.2	-4.79	-68.84	43.4	-25.44
Silychristin	-36.52	-205.98	200.23	-6.29	-242.49	193.95	-48.55
α-G							
Acarbose	-35.68	-503.74	510.36	-5.47	-539.42	504.88	-34.54
Hyperoside	-41.73	-63.29	74.67	-6.19	-105.02	68.48	-36.54
Silychristin	-37.9	-17.6	37.2	-5.24	-55.5	32	-23.5

VDWAALS: Van der Waals energy; EEL: Electrostatic energy; EGB: MMGBSA polar solvation energy; ESURF: MMGBSA nonpolar solvation energy; ΔG_GAS: Net gas phase energy; ΔG_SOLV: Net solvation energy; ΔG_TOTAL: Net system energy.

For α-G, the binding free energy analysis shows a different trend. Acarbose maintains a strong binding affinity with a total binding free energy (ΔTOTAL) of -34.54 kcal/mol. The binding is characterized by very strong electrostatic interactions (-503.74 kcal/mol) and moderate van der Waals interactions (-35.68 kcal/mol). Despite this, acarbose manages to maintain a strong interaction with α-G due to the dominance of its electrostatic

interactions. Hyperoside displays a slightly better binding affinity with α-G than acarbose, with a total binding energy (ΔTOTAL) of -36.54 kcal/mol. This stronger binding is mainly due to its robust van der Waals interactions (-41.73 kcal/mol) and a relatively lower polar solvation penalty (EGB: 74.67 kcal/mol) compared to acarbose. Although its electrostatic interactions (-63.29 kcal/mol) are not as strong as those of acarbose, the more favourable balance between gas-phase interactions (ΔG_GAS: -105.02 kcal/mol) and solvation effects results in a stable and effective binding interaction. Silychristin, on the other hand, exhibits the weakest binding affinity with α-G among the three inhibitors, with total free energy (ΔTOTAL) of -23.50 kcal/mol. It has moderate van der Waals interactions (-37.90 kcal/mol) and relatively weak electrostatic interactions (-17.60 kcal/mol). This suggests that silychristin is less effective in inhibiting α-G compared to acarbose and hyperoside.

5.5. Conclusion

This chapter provided a comprehensive evaluation of the antidiabetic potential of *Ichnocarpus frutescens* and *Hemidesmus indicus*, and isolated compounds, hyperoside and silychristin. In α-A inhibition assays, the methanol extracts of *Hemidesmus indicus* and *Ichnocarpus frutescens* showed the highest inhibition percentages of 92.57% and 72.25%, respectively, with significantly lower IC_{50} values (4.19 mg/mL for *Hemidesmus indicus* and 7.34 mg/mL for *Ichnocarpus frutescens*) compared to other solvent extracts. Similarly, in α-G inhibition assays, methanolic extracts were highly effective, showing inhibition percentages of 73.05% and 86.27%, with the lowest IC_{50} values (5.78 mg/mL and 4.40 mg/mL). Lineweaver-Burk plot analysis confirmed that methanol extracts of *Hemidesmus indicus* and *Ichnocarpus frutescens* act as competitive inhibitors for both α-A and α-G enzymes.

The isolated compounds, hyperoside and silychristin, demonstrated even more potent inhibitory effects against both α-A and α-G than the standard inhibitor acarbose. In α-A

inhibition assays, hyperoside and silychristin reached maximum inhibition rates of 78% and 69%, respectively, while acarbose achieved only 61%. For α-G, both hyperoside and silychristin exhibited superior inhibitory potentials compared to acarbose. Mode of inhibition studies revealed that acarbose and hyperoside act as competitive inhibitors of α-A, while silychristin follows an uncompetitive inhibition mechanism. For α-G, acarbose and silychristin exhibited competitive inhibition, whereas hyperoside displayed a non-competitive MOI.

Docking analysis supported these experimental findings, showing that hyperoside and silychristin have stronger binding affinities for both enzymes than acarbose. The BE for α-A were -6.65 kcal/mol for hyperoside and -8.98 kcal/mol for silychristin, compared to -4.71 kcal/mol for acarbose. For α-G, hyperoside and silychristin showed BE of -7.25 kcal/mol and -6.91 kcal/mol, respectively, surpassing acarbose's BE of -4.36 kcal/mol. Further MD analyses, including RMSD, RMSF, RoG, and SASA, confirmed that these enzyme-inhibitor complexes maintain a stable, compact structure with a higher proportion of alpha-helix and beta-sheet secondary structures. MM/GBSA analysis provided additional insights, indicating that silychristin has the highest binding affinity and inhibitory potential for α-A (ΔTOTAL: -48.55 kcal/mol). In comparison, hyperoside exhibited superior binding potential for α-G (ΔTOTAL: -36.54 kcal/mol).

Cytotoxicity studies on the 3T3-L1 cell line demonstrated that both silychristin and hyperoside exert dose-dependent inhibitory effects on adipocyte cells, with IC_{50} values of 129.66 µg/mL for silychristin and 40.60 µg/mL for hyperoside, suggesting that hyperoside is more potent. The NBDG glucose uptake assay further showed that both compounds significantly enhance glucose uptake in adipocytes, with silychristin inducing a 5.7-fold increase and hyperoside a 3.2-fold increase compared to untreated cells, highlighting their potential role in improving insulin sensitivity. Additionally, the wound

healing assay demonstrated the ability of silychristin and hyperoside to promote cell migration and wound closure. Untreated cells showed limited wound healing, while hyperoside-treated cells achieved 60% wound closure at 24 hours and 75% at 48 hours. Silychristin-treated cells exhibited an even more pronounced effect, with 70% wound closure at 24 hours and nearly 90% at 48 hours. These findings indicate that both compounds not only act as potent enzyme inhibitors but also support tissue repair and wound healing.

This chapter has highlighted the significant antidiabetic potential of the isolated compounds Hyperoside and Silychristin, demonstrating their effectiveness in managing diabetes and its complications. There is a well-established connection between diabetes and cancer, as both conditions share common underlying mechanisms, including chronic inflammation, altered insulin signalling, and metabolic dysfunction. Hyperglycemia and insulin resistance, which are characteristic of diabetes, have been associated with an increased risk of developing certain types of cancer. Elevated insulin levels and related growth factors can promote cancer cell proliferation, while metabolic imbalances may contribute to tumour progression. Therefore, the next chapter aims to explore the anticancer potential of the phytoconstituents Hyperoside and Silychristin, isolated from *Ichnocarpus frutescens* and *Hemidesmus indicus*.